Catalysis Science & Technology

ROYAL SOCIETY OF CHEMISTRY

PAPER

View Article Online
View Journal | View Issue

Check for updates

Cite this: *Catal. Sci. Technol.*, 2026, **16**, 962

Zinc alendronate as an ossified catalyst for glycerol valorization to glycerol carbonate using urea as a CO_2 surrogate

Shivani B. Thakkar,[a] Dinesh Bhalothia,[b] D. Krishna Rao[c] and Bibhas R. Sarkar*[a]

The conversion of biomass waste into valuable chemicals is a sustainable approach for a green and circular economy. Herein, the highly efficient solvent-free catalytic carbonylation of glycerol to glycerol carbonate ($GlyCO_3$) using cost-effective and facile ossified zinc alendronate catalysts and urea as a CO_2 surrogate is reported. Zinc alendronate catalysts were synthesized in a single step using an ossification technique. The catalysts were characterized by various techniques, including XRD, FT-IR spectroscopy, N_2 physisorption, TGA, SEM-EDS, TEM, XANES, XPS, NH_3- and CO_2-TPD, and multinuclear CP MAS NMR spectroscopy. Among the catalysts tested, ALN1Zn2 exhibited enhanced performance, achieving 86.3% glycerol conversion and 96.1% $GlyCO_3$ selectivity with 82.9% yield under optimized conditions (10% catalyst loading, 150 °C, 7 h, 1 : 1 glycerol to urea ratio). All products and byproducts were identified using GC-MS/MS analysis. The catalyst exhibited good reusability over multiple cycles with only slight activity loss. The reaction progress was monitored by FT-IR spectroscopy. Mechanistic studies indicated that the reaction proceeded *via* a carbamate intermediate. The bifunctional acid-base properties of the catalyst enabled the simultaneous activation of urea and glycerol. This work demonstrates a facile approach to develop efficient heterogeneous catalysts for sustainable glycerol valorization.

Received 13th October 2025,
Accepted 30th November 2025

DOI: 10.1039/d5cy01218j

rsc.li/catalysis

Introduction

The emphasis on the reduction of carbon footprint has led to substantial growth in the development of chemical routes from biomass-derived platform chemicals. The proliferation of the biodiesel and oleochemical industries has also led to the enhanced production of bio-based glycerol as a potential feedstock. Glycerol holds a major portion (~10%) of the total byproducts generated from the transesterification process during the biodiesel production from biomass.[1] The projected biodiesel production will reach 76 MMT by 2030.[2] It is anticipated that the global market value of glycerol, will reach USD 11.9 billion by 2034 (from USD 5.6 billion in 2024).[3] This projection necessitates the valorization of glycerol into value-added products to incorporate it into pharmaceutical, cosmetics, food and beverage (F&B), and other biochemical industries employing various processes like hydrogenolysis, dehydration, selective oxidation, carbonylation utilizing CO_2/CO and numerous other processes.[4] Among the various value-added products of glycerol, glycerol carbonate ($GlyCO_3$) holds great significance due to its diverse applications such as solvent, an electrolyte in dry batteries, a stabilizer in the paint industry, in resin production, for military purposes, and as a precursor in the polymer industry to manufacture polycarbonates, polyglycerol, polyurethanes and many more.[5] Furthermore, the significance of $GlyCO_3$ is evidenced by its projected market value of USD 2.4 billion in 2024, with an anticipated compound annual growth rate (CAGR) of 8.01% from 2022 to 2033.[6]

Several reaction pathways including the alcoholysis of urea with glycerol, transesterification with dialkyl carbonate, and carbonylation of CO_2/CO with glycerol have been investigated for the synthesis of $GlyCO_3$.[7] Among these pathways, the alcoholysis of urea with glycerol emerges as the most promising as it avoids the involvement of volatile and flammable substances (alcohols) and toxic reactants (CO) and is not constrained by any thermodynamic limitations (activation of CO_2).[8] The alcoholysis of urea with glycerol employs two cost-effective and accessible raw materials (glycerol and urea) to produce $GlyCO_3$. Ammonia gas, generated as a byproduct during this reaction, can be captured and subsequently utilized in urea production from CO_2;[9,10] thus, urea functions as a CO_2 surrogate and may be

---

[a] Department of Chemistry, Birla Institute of Technology and Science, Pilani, Pilani Campus, Vidya Vihar, Pilani, Rajasthan 333031, India.
E-mail: bibhas.sarkar@pilani.bits-pilani.ac.in
[b] Department of Electronics and Communication Engineering, Manipal University Jaipur, Rajasthan 303007, India
[c] Tata Institute of Fundamental Research Hyderabad, Hyderabad, Telangana,

considered to assist in CO_2 cycling from an overall process perspective. Thus, the alcoholysis of urea with glycerol offers a potentially ecofriendly and sustainable solution for the synthesis of $GlyCO_3$.

A variety of catalysts have been reported for the $GlyCO_3$ synthesis *via* the alcoholysis of urea with glycerol, including extensively investigated zinc-based catalysts [ZnO,[11] ZnO-mixed oxide catalysts,[12] supported Zn catalysts,[13] Zn^{2+}-incorporated catalysts,[14] other Zn-containing compounds,[15] *etc.*]; lanthanum-based catalysts [lanthanum oxide,[16] other La-compounds,[17,18] *etc.*]; tin-based catalysts [supported Sn or Sn-mixed oxide catalysts,[19] Sn-decorated heteropolyacids,[20] *etc.*]; phosphates;[9,10] ionic liquids;[21] hydrotalcite-like materials;[22] and various other types of catalysts [water-boiler ash,[23] metal salts,[24] *etc.*] Zn-based catalysts have garnered particular attention due to the ability of Zn to activate glycerol in the form of Zn glycerolate.[25] To facilitate the reaction, the Lewis acidity of Zn^{2+} can be used to activate the carbonyl group in urea.[26] Both homogeneous and heterogeneous types of Zn-based catalysts have been extensively investigated in recent years.

Solid Zn-based catalysts have attracted considerable interest owing to their comparatively high catalytic efficacy in glycerol carbonylation.[25–29] Nonetheless, investigations have revealed that reactions facilitated by these solid Zn catalysts actually progress homogeneously, rather than heterogeneously, as initially assumed.[25] The Zn species readily dissolves in the liquid medium *via* interaction with glycerol and urea, subsequently forming catalytically active zinc isocyanate ($Zn{-}N{=}C{=}O$) complexes.[15] This phenomenon occurs regardless of the original solid Zn catalyst type. A comprehensive analysis of the conversion rate, selectivity, and reusability underscores the need to develop more effective heterogeneous Zn-based catalytic systems.

Various Zn compounds [ZnF_2, $ZnCl_2$, $ZnBr_2$, ZnI_2, $Zn(NO_3)_2{\cdot}6H_2O$, $Zn(OAc)_2{\cdot}2H_2O$, ZnO, *etc.*] have been investigated as homogeneous catalysts to activate glycerol and urea.[15] Among these, homogeneous $ZnCl_2$ demonstrated ~80% glycerol conversion and ~99% $GlyCO_3$ selectivity.[15] Zinc glycerolate [$Zn(C_3H_6O_3)$] was identified as an active species in all these homogeneous Zn catalysts.[15] Zhang *et al.* examined $ZnSO_4$, $CuSO_4$, and $MgSO_4$ for the glycerolysis of urea to $GlyCO_3$, with $ZnSO_4$ exhibiting optimal performance with a 93% yield.[24] Homogeneous catalysts exhibited greater glycerol conversion and $GlyCO_3$ selectivity due to their enhanced contact/availability with the reagents during reactions.[8] Nevertheless, the application of homogeneous catalysts is constrained by catalyst-product separation, catalyst recovery, and economic reutilization. The approach of heterogenizing homogeneous catalysts can address separation issues, albeit often at the expense of their catalytic activities. Researchers have emphasized the significance of the availability of the acid-base dual functionality in a single catalyst for the alcoholysis of urea with glycerol, which effectively suppresses their mutual deactivation.[9,10] However, controlling these chemically divergent, hostile active sites remains a challenge. Furthermore, most of the synthesis strategies have notable disadvantages owing to exotic preparation procedures and multistep catalyst synthesis, which again limit these systems' actual application feasibility. Consequently, developing a facile method for synthesizing acid-base bifunctional catalysts with high activity and selectivity remains the most poignant challenge.

Metal phosphonates represent a significant class of hybrid materials, consisting of organic and inorganic moieties intimately integrated at the molecular level through P–O–metal covalent bonds, with a unique structural combination of the advantageous properties of both organic and inorganic moieties.[30–34] A wide range of functionalized phosphonic acids and their derivatives that are low-cost and have diverse functional groups can be utilized to synthesize metal phosphonates through various methods, including coprecipitation, sol–gel, and hydrothermal processes.[32,35] Notably, the uncoordinated free P–O–H groups on metal phosphonate materials exhibit exceptional acid properties.[30–32,34–36] Conversely, the incorporation of spacer alkyl groups with terminal tertiary amine species into the framework of metal phosphonates results in materials exhibiting nonalkaline/weakly alkaline basic properties.[33,34,36] Thus, amine-functionalized alkyl moieties present in the phosphonates of Zn may be proposed as prospective catalysts for the synthesis of $GlyCO_3$. Earlier, Sarkar *et al.*[37] introduced a novel approach called 'ossification' to synthesize intrinsically insoluble metal complexes with some of their coordinated ligands having appendages with chemical moieties that can form insoluble ion-pairs, where the catalytically active metal environment is kept intact for participating in catalytic reactions, and a different metal ion-pair forms a stable insoluble attribute. Thus, catalytically active metal-site-containing molecules are precipitated by a process resembling the self-assembly of robust insoluble biomaterials, such as bones, from simpler soluble precursor molecules and ions. The ossification technique thus offers a promising avenue for addressing the above-mentioned challenges.

This study aimed to synthesize zinc alendronate catalysts using an ossification technique and evaluate their efficacy and reusability in the alcoholysis of urea with glycerol to develop a more efficient and environmentally friendly catalytic process. This process utilized two phosphonates ($-PO_3^{2-}$) and an amino ($-NH_2$) group containing sodium alendronate trihydrate (Na-ALN, Scheme 1) as the crucial molecule, which can bind with Zn *via* the phosphonate (P–O–H) moiety preferably in an incomplete manner to leave residual acidity, while the free $-NH_2$ group provides basicity, in addition to forming insoluble Zn-phosphonate-based materials. Notably, Na-ALN is a potent osteoclast-mediated bone resorption inhibitor and is used as a

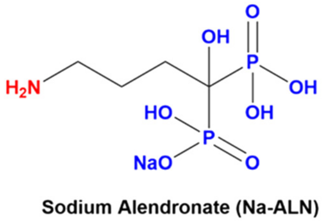

Scheme 1 Molecular structure of sodium alendronate (Na-ALN).

drug to treat osteoporosis.[38] Benefiting from the synergistic effect of the active acidic and basic sites, these materials can activate glycerol and urea simultaneously in a solvent-free system to yield $GlyCO_3$. Furthermore, the ossified catalyst material can be readily recovered by filtration and reused while maintaining its original activity.

Experimental methods

Materials and reagents

Sodium hydrogen (4-amino-1-hydroxy-1-phosphonobutyl) phosphonate trihydrate (alendronate sodium hydrate, 98%, BLD Pharma, India), zinc nitrate hexahydrate (99% (metal basis), Thermo Scientific Chemicals, India), glycerol anhydrous (>98%, Merck, India), urea (99%, Molychem, India) and methanol (≥99.8% (GC), Merck, India) were purchased and used without any further purification.

Synthesis procedure of the ossified zinc alendronate catalysts and their characterization methods

Initially, a weighted amount of alendronate sodium trihydrate (Na-ALN) was ultrasonicated in 10 mL of water to prepare a 0.1 M homogeneous aqueous solution of Na-ALN. A prepared zinc nitrate solution was added to 10 mL of a 0.1 M aqueous solution of Na-ALN dropwise with stirring at different Na-ALN/Zn molar ratios, ranging from 0.5 to 1 and 2. The pH of the Na-ALN solution was 3.9. The pH of the final solution varied between 4.5 and 6.2, depending on the molar ratio of Na-ALN/Zn. The mixture was maintained at 80 °C for five days under stirring conditions. The solid was recovered and washed several times with deionized water to remove any remaining unreacted Na-ALN or zinc and subsequently dried at 70 °C overnight. All the samples were stored in a dry environment. The solids prepared using Na-ALN/Zn at molar ratios of 0.5, 1, and 2 were labelled as ALN1Zn2, ALN1Zn1, and ALN2Zn1, respectively, and called ossified zinc alendronate catalysts. The final pH values of the ALN1Zn2, ALN1Zn1, and ALN2Zn1 solutions after five days were 0.6, 1.36, and 2.31, respectively. As quantified by AAS analysis, the Zn loadings in ALN1Zn2, ALN1Zn1, and ALN2Zn1 were 11.28, 10.64, and 5.02 wt%, respectively.

Catalyst structural and morphological analyses were done employing various techniques, including powder X-ray diffraction (PXRD), Fourier transform infrared (FT-IR) spectroscopy, field-emission scanning electron microscopy (FESEM) coupled with energy-dispersive X-ray spectroscopy (EDS), high-resolution transmission electron microscopy (HR-TEM), nitrogen (N_2) physisorption, X-ray photoelectron spectroscopy (XPS), thermogravimetric analysis (TGA), NH_3- and CO_2 temperature-programmed desorption (NH_3- and CO_2-TPD), solid-state NMR (SS-NMR) spectroscopy and extended X-ray absorption fine structure (EXAFS). Detailed characterization methodologies are provided in the SI.

Liquid-phase glycerolysis of urea and identification of products

The alcoholysis of urea with glycerol was carried out in a 50 mL two-neck round-bottom flask. Initially, 2 g (22 mmol) of glycerol was added to the flask and heated to 140 °C (or up to the required temperature) to reduce its density. Subsequently, 0.2 g of the catalyst (or the required amount of the catalyst) was incorporated into glycerol under continuous stirring. After the uniform distribution of the catalyst in glycerol, 1.3 g (22 mmol) of urea (or the required amount of urea) was introduced into the reaction mixture. The reaction was conducted under a continuous N_2 flow (20 mL min^{-1}) to remove the generated ammonia gas during the reaction with constant agitation in a reflux setup. The synthesized products were identified using GC-MS/MS and quantified with gas chromatography (GC). The detailed product analysis and identification are provided in the SI.

Results and discussion

Catalyst structural and morphological characterization

Powder X-ray diffraction (PXRD) analysis was performed in the 2θ range from 5° to 40° to identify the crystallinity and phase composition of the synthesized catalysts, as presented in Fig. 1a. The presence of multiple diffraction peaks confirmed the crystalline nature of the catalyst. The diffraction patterns of commercially available sodium alendronate, Na-ALN, were recorded and compared with those of the synthesized zinc alendronate catalysts (namely, ALN1Zn2, ALN1Zn1 and ALN2Zn1). Notably, the diffraction peaks deviated slightly from the standard JCPDS data of Na-ALN (JCPDS 00-050-2301) due to the presence of varying amounts of water of crystallization in the commercially available Na-ALN.[39,40] As illustrated in Fig. 1a, the intense diffraction peaks at 2θ values of 8.6°, 11.9°, 13.1°, 16.7°, 18.2°, 22.8°, 24.4°, 25.6°, and 29.4° corresponded to the (002), (101), (012), (−112), (044), (−114), (−122), (015), and (123) crystallographic planes, respectively, of Na-ALN (JCPDS 00-050-2301).[39,40] Upon the reaction of zinc with Na-ALN, peaks related to zinc pyrophosphate ($Zn_2P_2O_7$) (JCPDS 00-007-0087) were observed in the ossified zinc alendronate catalysts. The additional peaks at 17.2° (200) and 20.4° (−111) in the case of ALN1Zn2, 15.8° (011) and 17.5° (200) for ALN1Zn1 and 14.9° (−111) and 17.4° (200) for ALN2Zn1 respectively, were associated with different forms of zinc phosphonate [$Zn_3(PO_3)_4$, (JCPDS 00-021-1488 and 00-021-1489)], indicating the formation of polyphosphate phases in the ossified zinc alendronate catalysts. The diffraction peaks at 8.6°, 16.6°, 22.9°, 26.4°, and 33.4° in ALN1Zn2 and 11.6°, 12.2°, 23.3°, and 26.4° in both ALN1Zn1 and ALN2Zn1 shifted relative to those of pure Na-ALN (Fig. 1a). These shifts were attributed to the probable formation of phosphonate bonds between zinc and Na-ALN. The diffraction pattern trends revealed that as the zinc concentration decreased from ALN1Zn2 to ALN1Zn1 and further to ALN2Zn1, Zn-ALN integrated easily alongside Na-ALN. This integration

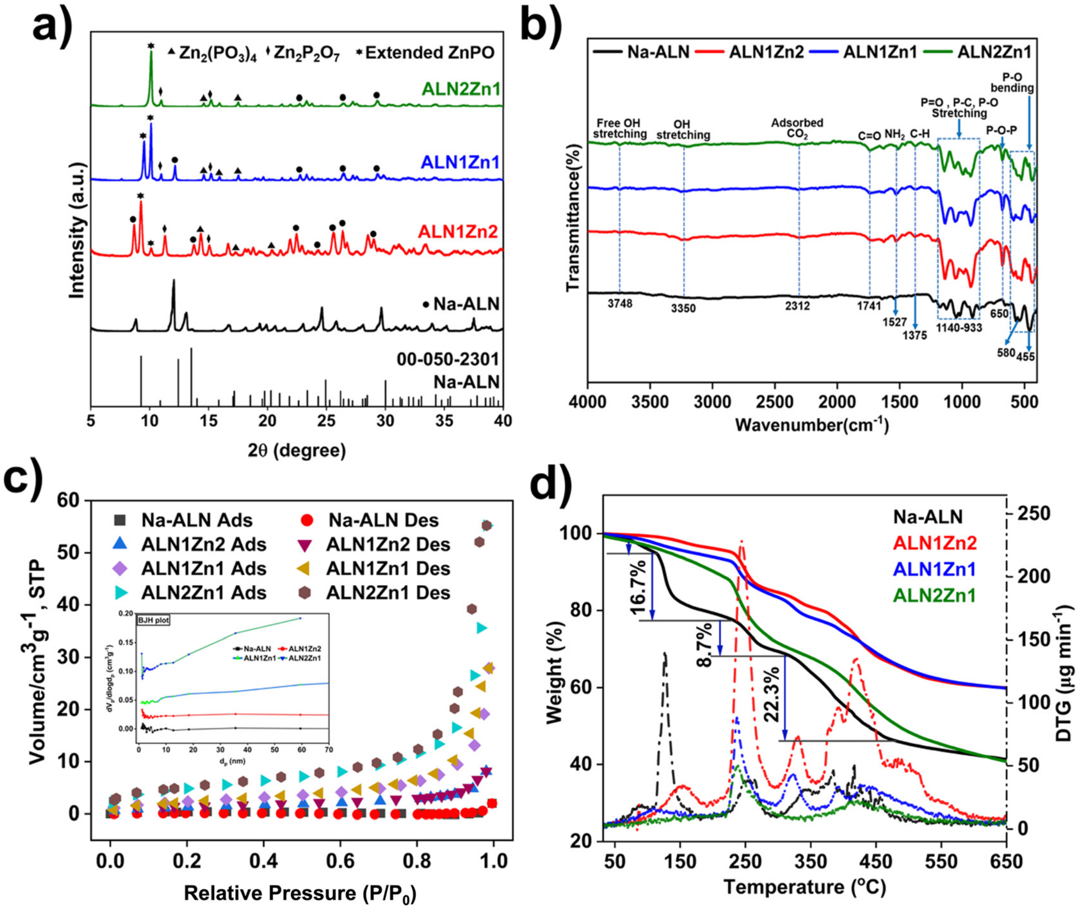

Fig. 1 a) PXRD patterns, b) FT-IR spectra, c) N_2 physisorption plots and BJH pore size distribution plots (inset), and d) TGA spectra of Na-ALN and ossified zinc alendronate catalysts.

promoted the development of pyrophosphate-type geometries in the ossified catalysts. Therefore, the PXRD analysis clearly indicates the formation of mixed phosphonate phases in the ossified zinc alendronate catalyst.

The FT-IR spectra of Na-ALN and the ossified zinc alendronate catalysts were obtained and are shown in Fig. 1b. The ossified zinc alendronate catalysts exhibited absorption bands similar to those of Na-ALN. The presence of the 3748 cm^{-1} band was related to the free hydroxyl group (OH)[41] in Na-ALN and the ossified zinc alendronate catalysts. The band at approximately 3350 cm^{-1} was attributed to hydrogen-bonded OH (from water hydration) or N–H stretching vibrations (from NH_2 groups).[42] In the case of bisphosphonate materials, atmospheric CO_2 adsorption on the catalyst surface was observed at 2312 cm^{-1}.[43] The absorption band centered at 1741 cm^{-1} could be attributed to C=O stretching due to CO_2 adsorption. This phenomenon may have occurred because of the presence of oxygen or the oxygen anions from adjacent sodium alendronate units available for interaction. At 1527 cm^{-1}, the NH_2 groups exhibited a distinctive absorption peak associated with the N–H bending vibration.[44] The spectra show C–H symmetric bending vibrations at 1375 cm^{-1}.[45] The bands at 1140, 1063, and 933 cm^{-1} were linked to the P=O, P–C, and P–O stretching vibrations, respectively.[44,46] Subsequently, the band at 650 cm^{-1} corresponded to the P–O–P vibrations.[41] The intensity of the band at 650 cm^{-1} for the ossified zinc alendronate catalysts was significantly higher than that for Na-ALN, which is related to zinc-phosphonate interactions. Finally, the deformation mode of P–O- resulted in peaks at 580 cm^{-1} (ref. 47, 48) and Zn–O vibrations at 455 cm^{-1}, respectively.[47,49] Consequently, these observations offer a comprehensive view of the bending and stretching modes of P–O–P, C–H, NH_2, and C=O bonds that are present in the ossified catalysts after synthesis.

Surface analysis using N_2 physisorption at cryogenic temperatures (77 K) was performed to comprehend the texture (surface area and porosity) of the synthesized materials. The surface areas of the synthesized materials were calculated using the Brunauer–Emmett–Teller (BET)[50] method. Simultaneously, the mesopore size distribution (~2–13 nm)[51] (Table. 1) was assessed by the Barrett–Joyner–Halenda (BJH)[50] method using the Harkins–Jura standard isotherm. The adsorption–desorption isotherms of Na-ALN and the ossified zinc alendronate catalysts revealed a IUPAC type IV (a)[51,52] isotherm with a vertically oriented inverted horn-shaped hysteresis classified as semi-IUPAC H1 hysteresis[50–52] (Fig. 1c). The resulting adsorption–desorption

Table 1 BET analysis of Na-ALN and ossified catalysts

Catalyst	$a_{S,BET}$ (m^2 g^{-1})	Total pore volume (cm^3 g^{-1})	Avg. pore diameter (nm)
Na-ALN	1.49	0.0008	1.90
ALN1Zn2	5.29	0.0098	6.06
ALN1Zn1	8.92	0.0432	12.5
ALN2Zn1	17.8	0.0646	8.90

of the catalysts showed an inflection point at P/P_0 ~ 0.93,[52] and hysteresis started at P/P_0 ~ 0.63,[52] followed by a plateau (Fig. 1c). Table 1 demonstrates an increase in the specific surface area and total pore volume with decreasing zinc concentration, suggesting a higher prevalence of bisphosphonate sites. The presence of multiple pore diameters could be attributed to the disarrayed pore size distribution on the catalyst surface.[9]

The TGA-DTG curves of Na-ALN and the ossified catalysts are shown in Fig. 1d, which exhibit four major weight loss regions. Na-ALN exhibited two weight losses between 50 and 200 °C (ref. 40, 46) (Fig. 1d). The first thermal event was associated with the loss of adsorbed water on the surface.[40,46]

The second thermal event was endothermic in nature, as shown in the DTA results (Fig. S1), which corresponded to the loss of three chemically bound water molecules[40] (16.7%, which matches with the actual amount of water (16.6%) in Na-ALN) from the Na-ALN crystal with an onset temperature of 128 °C (Fig. 1d). Beyond 200 °C, a series of weight losses occurred, corresponding to the breakdown of the aliphatic chain or nitrogen groups[46] and the decomposition of the remaining organic and phosphonate groups (8.7% and 22.3%), leaving behind stable inorganic residues. Remarkably, after the ossification of zinc with Na-ALN, the catalysts were more thermally stable than Na-ALN (Fig. 1d). The ossified ALN1Zn2 catalyst exhibited the highest stability, according to the TGA-DTG analysis. The deep endothermic curve between 220 and 280 °C in the DTA analysis (Fig. S1) signified that a significant amount of heat was required to break the skeleton of the ossified catalyst after zinc coordination. This clearly indicates the greater stability of the ossified catalysts compared to Na-ALN, specifically in the cases of ALN1Zn2 and ALN1Zn1. However, the weight loss patterns/events of the ossified catalysts were similar to those of Na-ALN in terms of the thermal removal of adsorbed water and crystalline water and the degradation of aliphatic chains, including nitrogen-containing groups and phosphonate moieties, with logical variations owing to the complexity of the structure of the catalysts after zinc coordination.

The FESEM images of the synthesized catalyst samples are shown in Fig. 2a–d and S2–S4. The particles were irregular in shape. No specific surface morphology was observed for the ossified zinc alendronate catalysts. In addition, energy-dispersive X-ray analysis demonstrated the presence of elements in the ossified zinc alendronate catalysts (Fig. 2f and S2–S4). The presence of zinc was confirmed by the map sum spectrum (Fig. 2e shows ALN1Zn2; for ALN1Zn1 and ALN2Zn1, see Fig. S2–S4) and elemental mapping (for ALN1Zn2, see Fig. 2f; for ALN1Zn1 and ALN2Zn1, see Fig. S2–S4). The HR-TEM image and SAED pattern of ALN1Zn2 are displayed in Fig. 2h and g, and the images of ALN1Zn1 and ALN2Zn1 are given in Fig. S5 and S6, respectively. The SAED pattern displayed distinct concentric rings, indicating the polycrystalline nature of the material. The SEM images showed irregular-shaped particles with some degree of agglomeration. HR-TEM images further confirmed the presence of an elongated rod-like morphology with a uniform diameter and length, implying anisotropic growth during synthesis. These morphological characteristics, combined with the diffraction data, support the formation of a well-crystallized structure.

To gain deeper insights into the local coordination environment and electronic structure of Zn atoms in the experimental samples, X-ray absorption near-edge structure (XANES) spectroscopy was employed. Fig. 3a presents a comparative analysis of the Zn K-edge XANES spectra of the

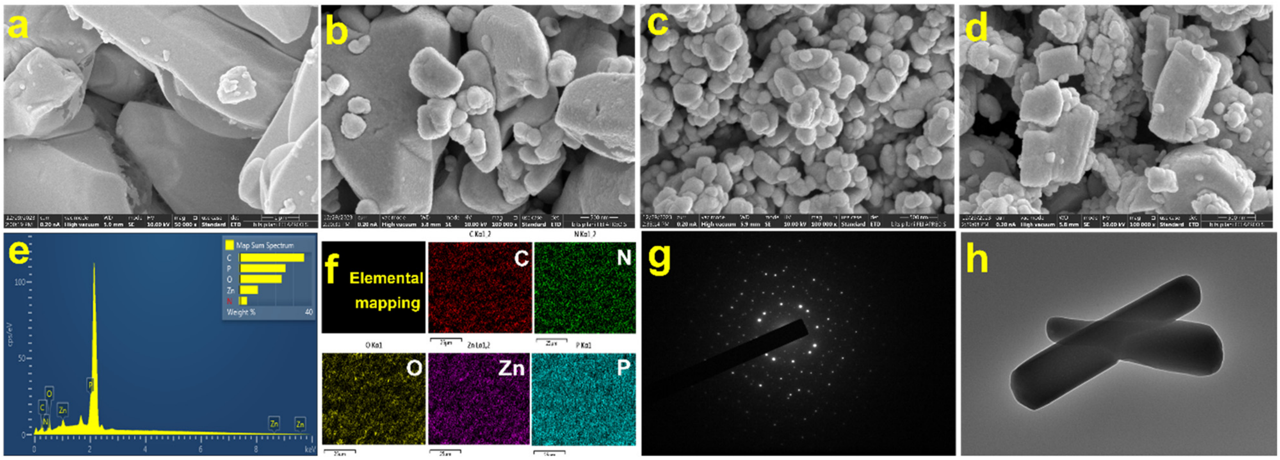

Fig. 2 FESEM images of a) Na-ALN, b) ALN1Zn2, c) ALN1Zn1, and d) ALN2Zn1, e) map sum spectrum of ALN1Zn2, f) elemental analysis of ALN1ZN2, g) SAED pattern of ALN1Zn2, and h) HR-TEM image of ALN1Zn2.

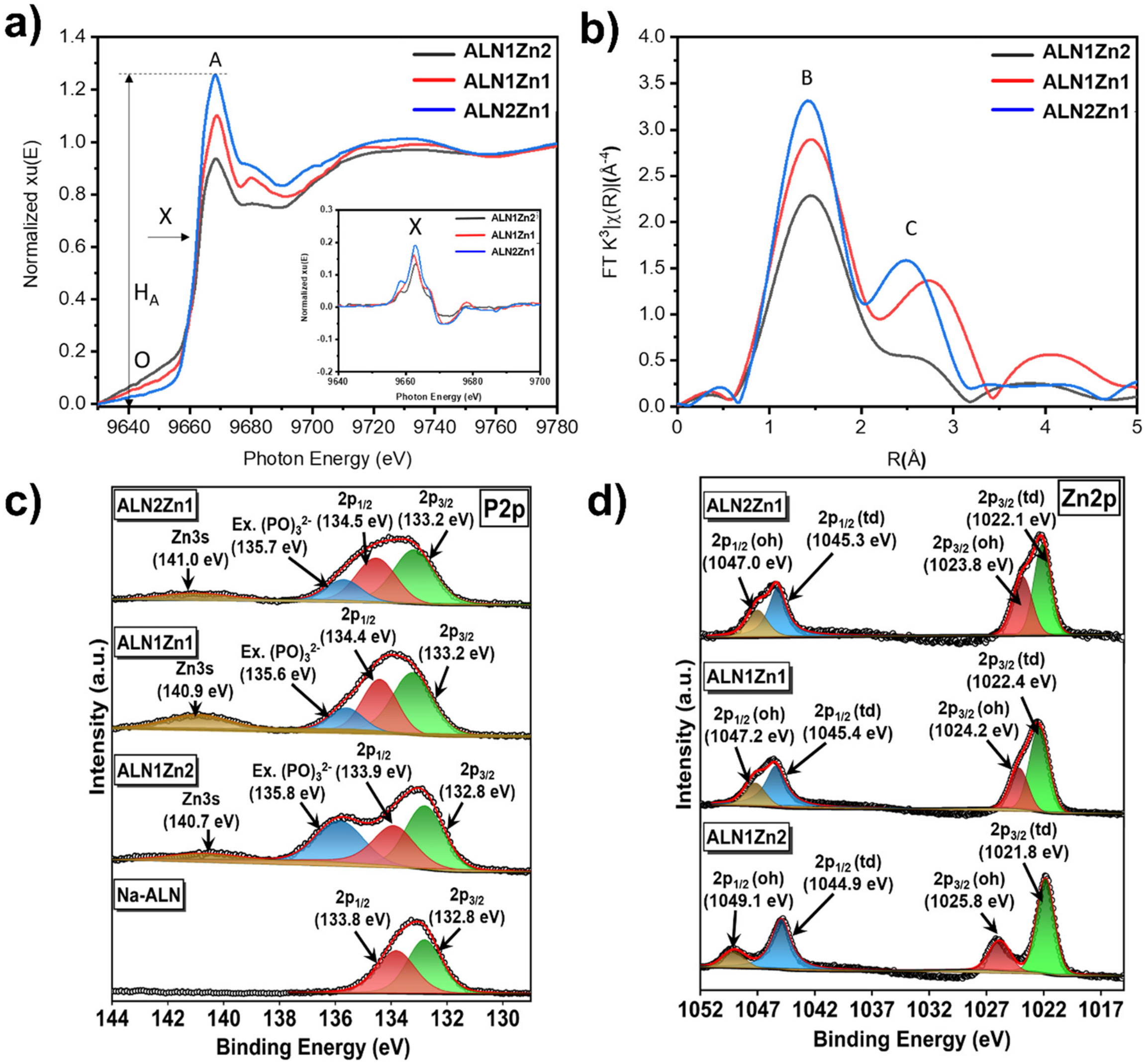

Fig. 3 X-ray absorption spectroscopy of the experimental samples. a) XANES and b) FT-EXAFS spectra of the experimental samples at the Zn K-edge. The first derivative spectra are shown in the inset of the XANES spectra. c) Deconvoluted P 2p XPS and d) deconvoluted Zn 2p XPS spectra of Na-ALN and ossified zinc alendronate catalysts.

samples. Several prominent spectral features were observed and interpreted to understand the local atomic configuration of Zn in the respective materials. The pre-edge feature, labelled as "O," reflects the degree of local symmetry distortion around the absorbing Zn atom. This peak originates from the 1s → 3d electronic transition, which is typically dipole-forbidden in perfectly centrosymmetric (octahedral) environments but becomes allowed when the symmetry is distorted, such as in tetrahedral or square-planar geometries. The more pronounced pre-edge feature in ALN1Zn2 suggests that the Zn centers possess a distorted tetrahedral geometry. The position of the inflection point (denoted "X") in the absorption edge is commonly used to estimate the oxidation state of the absorbing atom. The similar position of the inflection point (peak X in the first derivative spectra) in all the samples confirmed the similar oxidation of Zn in all the samples. Furthermore, the intensity of the whiteline peak (labelled "H_A"), which corresponds to transitions from the Zn 1s core level to unoccupied 4p states, provides information about the density of unoccupied states above the Fermi level. The lowest H_A value for the ALN1Zn2 sample suggests the highest density of occupied orbitals in this sample. Such a scenario can be attributed to the highest interaction of Zn with adjacent domains in the ALN1Zn2 sample.

The Fourier-transformed EXAFS (FT-EXAFS) spectra of the samples further revealed the local structural environment around Zn atoms (Fig. 3b), and the corresponding structural parameters are summarized in Table S1. In the FT-EXAFS spectra, peak B (~1.5–2.0 Å) corresponded primarily to Zn–O interactions and showed the lowest amplitude for ALN1Zn2, indicating the lowest extent of surface adsorbed oxygenated species on Zn in this sample, which is in good agreement with the whiteline intensity in the XANES spectra (Fig. 3a). The highest intensity of peak B indicates a more well-ordered and stronger Zn–O bonding environment in ALN1Zn2 than ALN1Zn1 and ALN2Zn1. This is further supported by the

EXAFS-derived coordination numbers (CN), where the Zn–O CN is highest in ALN1Zn2 (2.40) and gradually decreases to 1.84 in ALN2Zn1. Peak C (~3.0–3.5 Å) represented overlapping contributions from Zn–Zn, Zn–P, and Zn–OH interactions. Samples ALN1Zn1 and ALN2Zn1 displayed increased Zn–OH coordination and more pronounced Zn–P bond length contraction, indicating a distorted and more disordered Zn environment. These findings highlight that ALN1Zn2 possesses the most well-defined and structurally stable Zn coordination environment, which is likely to enhance its catalytic performance relative to that of the other samples.

X-ray photoelectron spectroscopy (XPS) was performed to ascertain the chemical environment and oxidation state of the elements present on the surface of the synthesized catalyst. The XPS survey spectra (Fig. S7) and C 1s (Fig. S8a, Table S2), N 1s (Fig. S8b, Table S2), O 1s (Fig. S8c, Table S2), P 2p (Fig. 3c, Table S2), and Zn 2p (Fig. 3d, Table S2) XPS profiles of the ossified zinc alendronate catalysts and pure Na-ALN provided a glimpse into the electronic environment of the surrounding atoms. The C 1s XPS spectra of Na-ALN, ALN1Zn1, and ALN1Zn2 showed three peaks, while four peaks were observed for ALN2Zn1 (Fig. S8a, Table S2). The signal at 284.8 eV in the C 1s XPS spectrum was attributed to the C–C/C–H (ref. 53, 54) bonds of the alkyl chain of Na-ALN. The peak of the C–N bond from the amine group[55,56] in alendronate was observed at 286.2, 286.1, 286.1, and 286.2 eV for Na-ALN, ALN1Zn2, ALN1Zn1, and ALN2Zn1, respectively. Notably, the binding energy of the C atoms in the C–P–O bonded species appeared to be highly affected by the coordination of zinc with the electron-withdrawing oxygen atoms of the two phosphonate groups. In Na-ALN, the P–O bonded C-species was observed at 288.6 eV. The higher binding energy with respect to the adventitious carbon was due to the highly electron-withdrawing phosphonate unit (two counts) lowering the electron density on the C atom.[57,58] As more and more zinc was coordinated to the phosphonate unit, this was partially compensated for, and a consequent trend of the lowering of the C 1s binding energy was observed as follows: ALN2Zn1 (288.5 eV), ALN1Zn1 (287.8 eV), and ALN1Zn2 (287.9 eV), all data following the reports by Puziy *et al.* (2008).[57,58] Additionally, a very-low-intensity[59,60] peak was observed in the C 1s spectrum of ALN2Zn1 at 290.2 eV, which may be attributed to the presence of the O–C═O species[59,60] because of CO_2 adsorption from the atmosphere, similar to that observed by Saeb *et al.* (2017)[59] and Gouzman *et al.* (2006).[60] This result corroborates the FT-IR spectra. This indicates that a higher zinc content may facilitate stronger CO_2 adsorption, and this effect was not detected for catalysts with lower Zn contents.

The main peaks at 401.1 eV (Na-ALN), 401.4 eV (ALN1Zn2) and 401.7 eV (ALN1Zn2, ALN1Zn1) in the N 1s XPS profiles (Fig. S8b, Table S2) indicated the presence of free or weakly interacting amine nitrogen[61] from the alendronate moiety. Moreover, the 402.0 eV peak in the N 1s spectrum of Na-ALN (Fig. S8b, Table S2) implied a protonated amino group ($-NH_3^+$).[58,62] The shift in the N 1s binding energies of the ossified zinc alendronate catalysts (Fig. S8b) compared with Na-ALN was linked to the protonated nitrogen in ammonium moiety ($-NH_3^+$).

The deconvoluted O 1s XPS spectrum showed three peaks for the Na-ALN and ossified zinc alendronate catalysts (Fig. S8c and Table S2, respectively). The first set of peaks (at 531.1 eV for ALN1Zn2 and 531.6 eV for Na-ALN, ALN1Zn1, and ALN2Zn1) corresponded to the oxygen atoms in the phosphonate groups (P–O/P═O)[33,63] (Fig. S8c, Table S2). The binding energy in ALN1Zn2 (531.1 eV) was slightly lower than that in Na-ALN, suggesting a significant interaction between zinc and oxygen atoms (P–O–Zn).[33] The second set of peaks was indicative of the O atom in the hydroxyl moiety C–OH (ref. 33, 63) at 532.6 eV for ALN1Zn2 and 533.1 eV for Na-ALN, ALN1Zn1, and ALN2Zn1. The higher zinc content in ALN1Zn2 matched the lower binding energy, indicating more O–Zn ionic bonding with an anionic oxide-type ligation/bonding. The higher-binding-energy peaks (534.6–535.9 eV) in the O 1s XPS spectra were attributed to water molecules.[54,58,63] With increasing amounts of zinc in the ossified zinc alendronate catalysts (zinc amount: ALN1Zn2 > ALN1Zn1 > ALN2Zn1), the phosphonate and water oxygen atoms showed a more significant decrease in binding energies owing to the stronger interaction with zinc, as the zinc coordination increased the electron density around the oxygen, which lowered the binding energy.

The two peaks at lower binding energies (132.8–133.2 eV and 133.8–135.8 eV)[38,54,64] (Fig. 3c, Table S2) in the P 2p XPS spectra corresponded to the spin-orbit splitting of $2p_{3/2}$ and $2p_{1/2}$ (at a difference of 0.8–1.2 eV)[38,54] (Fig. 3c, Table S2) of phosphorus atoms within the phosphonate ($C-PO_3$) groups present in the compounds. These peaks are characteristic of phosphorus in the +5 oxidation state.[65] The absence of the ~135.6 eV peak[58,66] in the P2p XPS spectrum of Na-ALN compared to that of the ossified zinc alendronate catalysts was attributed to the presence of phosphorus in a more strongly coordinated environment. These higher-binding-energy peaks (~135.6 eV) in the P2p XPS spectra corroborate the formation of the pyrophosphate species-like[57,66] structure of catalysts with increasing ALN/Zn ratio (ALN/Zn: $0.5 < 1 < 2$), in agreement with PXRD data. Additionally, the zinc present in the ossified catalysts gave rise to the Zn 3s signals at 140–141 eV, as displayed in the P 2p XPS spectra (Fig. 3c).[67,68]

The Zn 2p binding energies were influenced by the coordination environment and oxidation state of the zinc species and transitions between tetrahedral and octahedral configurations in the ossified zinc alendronate catalysts (Fig. 3d, Table S2). Zinc in an octahedral coordination frequently exhibits higher binding energies than its tetrahedral counterpart due to an increased electron density in the octahedral environment, resulting in enhanced electron shielding. Therefore, tetrahedral environments were observed around 1021–1022.5 eV and 1044–1046 eV owing to $2p_{3/2}$ (td) and $2p_{1/2}$ (td), respectively.[69,70] By contrast, octahedral environments were noticed around 1023–

Table 2 Surface concentration (in%) of elements in different ossified zinc alendronate catalysts and Na-ALN from XPS analysis

	C	N	O	P	Na	Zn	Zn/P
Na-ALN	59.14	2.18	29.65	6.52	2.51	—	—
ALN1Zn2	40.33	4.73	34.18	11.42	0.27	9.07	0.79
ALN1Zn1	46.42	4.32	33.5	9.4	0.16	6.2	0.66
ALN2Zn1	58.48	2.53	29.22	6.2	0.1	3.47	0.56

1026 eV and 1047–1049 eV (ref. 71) due to $2p_{3/2}$ (oh) and $2p_{1/2}$ (oh), respectively,[69,72] in the ossified zinc alendronate catalysts (Fig. 3d). The exceptionally high binding energies in the Zn2p XPS profile of the ossified zinc alendronate catalysts confirmed the +2 oxidation state[73] of zinc ions and the highly electron-deficient environment due to more nuanced arrangements of molecules in the solid catalyst structure.

The surface atomic concentrations are listed in Table 2, which provides significant insights into the structure of the surface of the ossified zinc alendronate catalysts obtained through XPS analysis. With an increase in the concentration of zinc (zinc concentration: ALN1Zn2 > ALN1Zn1 > ALN2Zn1), the atomic concentrations of zinc, phosphorous, and oxygen on the catalyst surface increased (Table 2). These results suggest that a greater number of active zinc phosphate complexes are formed. Because the synthesized materials are all macroscopic and obtained as bulk precipitates with low surface areas and porosities, it is highly probable that the solid precipitate particles have almost similar bulk compositions. Additionally, sodium ions associated with Na-ALN remained in the catalysts in one form or another.

NH_3- and CO_2-TPD analyses were performed to evaluate the types of active sites (acidic and basic sites, respectively) on the catalyst surface, thereby understanding the mechanism involved in glycerol conversion, as presented in Fig. S9 and S10 and Table 3. The TPD experimental results were deconvoluted into Gaussian peaks[74] to overcome the limitations of qualitative comparisons between the NH_3- and CO_2-TPD patterns of the various ossified zinc alendronate catalysts (including Na-ALN as a reference) using a mathematical fitting program. The deconvolution process was performed based on the assumption that the NH_3 and CO_2 desorption activation energies followed a normal distribution, representing the heterogeneity associated with the adsorption sites on the analyte surface.[75,76] The deconvoluted peaks were distributed among three categories of sites: weak (<250 °C), moderate (250 to 400 °C), and strong (>400 °C), according to the NH_3 and CO_2 desorption temperature[74–76] (Table 3). The acidic sites (observed *via* NH_3-

Table 3 Types of acidic and basic sites from NH_3- and CO_2-TPD analyses

NH_3-TPD (acidic sites)

	Weak (<250 °C)		Moderate (250 °C to 400 °C)		Strong (>400 °C)	
Catalyst	Temperature (°C)	Amount (mmol $g_{cat.}^{-1}$)	Temperature (°C)	Amount (mmol $g_{cat.}^{-1}$)	Temperature (°C)	Amount (mmol $g_{cat.}^{-1}$)
Na-ALN	152	2.2	313	6.0	438	1.5
	224	1.6	387	5.0		
ALN1Zn2	181	0.9	269	0.4	438	0.4
			295	2.2	510	1.3
			339	3.7		
			388	5.7		
ALN1Zn1	201	0.4	284	2.4	478	1.6
	249	0.9	332	5.4		
			396	3.1		
ALN2Zn1	224	2.0	305	1.4	488	1.5
			394	0.3		

CO_2-TPD (basic sites)

	Weak (<250 °C)		Moderate (250 °C to 400 °C)		Strong (>400 °C)	
Catalyst	Temperature (°C)	Amount (mmol $g_{cat.}^{-1}$)	Temperature (°C)	Amount (mmol $g_{cat.}^{-1}$)	Temperature (°C)	Amount (mmol $g_{cat.}^{-1}$)
Na-ALN	163	0.3	322	1.1	401	0.5
	236	0.3			493	0.1
ALN1Zn2	222	0.08	278	0.2	403	0.9
			348	0.6	454	0.02
					511	0.2
ALN1Zn1	193	0.07	277	0.3	423	0.5
			340	0.7	515	0.01
					570	0.4
ALN2Zn1	—	—	273	0.3	417	0.4
			371	0.3	501	0.1
			399	0.1		

Table 4 Comparison of the A/B ratio of the catalysts

	Total acidic sites (mmol $g_{cat.}^{-1}$) (A)	Total basic sites (mmol $g_{cat.}^{-1}$) (B)	A/B ratio
Na-ALN	16.3	2.3	7.09
ALN1Zn2	14.6	2.0	7.3
ALN1Zn1	14.1	1.98	7.1
ALN2Zn1	5.2	1.2	4.3

TPD) were likely related to the proton-donating capacity[77] of the hydroxyl (P–OH, C–OH), alkyl amine ($-NH_2$), and $-PO_3^{2-}$ structural components, including the influence of water molecules on the solid catalyst surface and the Zn coordination present in the catalyst structure. The weak acidic sites (<250 °C) in the Na-ALN and ossified zinc alendronate catalysts (Fig. S9, Table 3) represented physically (or weakly bound) adsorbed NH_3, which is mainly associated with surface-bound water and weakly interacting phosphonate groups in the NH_3-TPD. Meanwhile, the moderate acidic sites (250 to 400 °C) contributed significantly to the total acidity in all the catalysts (Fig. S9, Table 3), where NH_3 was bound tightly. These sites may be from partially deprotonated phosphonate and hydroxyl groups. Finally, the strong acidic sites (>400 °C) (Fig. S9, Table 3) in the catalysts corresponded to the strong interaction of NH_3 with the undissociated phosphonate groups in Na-ALN and the phosphonate groups bound to zinc ions in the ossified zinc alendronate species. A balanced distribution of acidic sites with a slight dominance of moderate acidity was observed in the NH_3-TPD of Na-ALN (Table 3). The ossified ALN1Zn2 and ALN1Zn1 exhibited higher concentrations of moderate and strong acidic sites (Table 3), reflecting the complex coordination of zinc ions with undissociated phosphonate groups. The presence of a greater number of strong acidic sites in ALN1Zn2 is consistent with the highest binding energy of zinc in an octahedral environment from the Zn2p XPS analysis. The nuanced coordination of Na-ALN and water molecules creates a high electron deficiency on zinc ions, which agrees with the strong acidity in the catalyst. In contrast, ALN2Zn1 had fewer acidic sites (Table 3), which leads to a less acidic character.

The presence of basic sites was examined through TPD utilizing CO_2 molecules as a probe. The deconvoluted CO_2-TPD peaks are shown in Fig. S10 and listed in Table 3 for Na-ALN and the ossified zinc alendronate catalysts. The existence of adsorbed water or loosely bound oxygen atoms[78] on the solid catalyst surface, the lone pair of nitrogen atoms in the amino group,[26] and the oxygen atoms in phosphonate groups ($-PO_3^-$) in the catalyst structure cumulatively gave rise to weak (<250 °C), moderate (250 °C to 400 °C), and strong (>400 °C) basic sites in the CO_2-TPD profiles. Notably, the basicity of the ossified zinc alendronate catalysts and Na-ALN was significantly lower than their acidity (Tables 3 and 4). The absence of electropositive metal centers explains the highest basicity of Na-ALN. The total number of basicities decreased after the complexation of zinc with Na-ALN (Table 3). To compare the acidic and basic strengths of the catalysts, the A/B ratio (total acidity/total basicity) was calculated (Table 4). The following trend was observed: ALN1Zn2 > ALN1Zn1 > Na-ALN > ALN2Zn1, which means that ALN1Zn2 is the most acidic among all, with an A/B ratio of 7.3 and a total acidity of 14.6 mmol g^{-1} (Table 4). In this regard, the ossified zinc alendronate catalysts revealed bifunctionality with the presence of acidic and basic sites in the same catalyst with different strengths of acidity and basicity in NH_3- and CO_2-TPD, respectively.

As shown in Fig. 4a and b, the Na-ALN sample exhibited well-resolved J (^{13}C–^{31}P)-coupled ^{13}C and ^{31}P spectra following ^1H decoupling. All resonance signals corresponding to the Na-ALN molecule could be unambiguously assigned. However, upon the introduction of zinc, noticeable distortion appeared in both the ^{13}C and ^{31}P signals. This spectral distortion remained consistent across samples with equimolar or excess zinc relative to ALN. The sample containing excess ALN displayed intermediate spectral features lying between those of pure ALN and the ALN–Zn complex. These observations suggest a strong interaction between zinc and phosphorus atoms, which likely alters the dihedral angles of the ALN molecule upon complexation with zinc.

Glycerolysis of urea

The catalytic performance of the ossified zinc alendronate catalysts was investigated for the solvent-free glycerolysis of urea

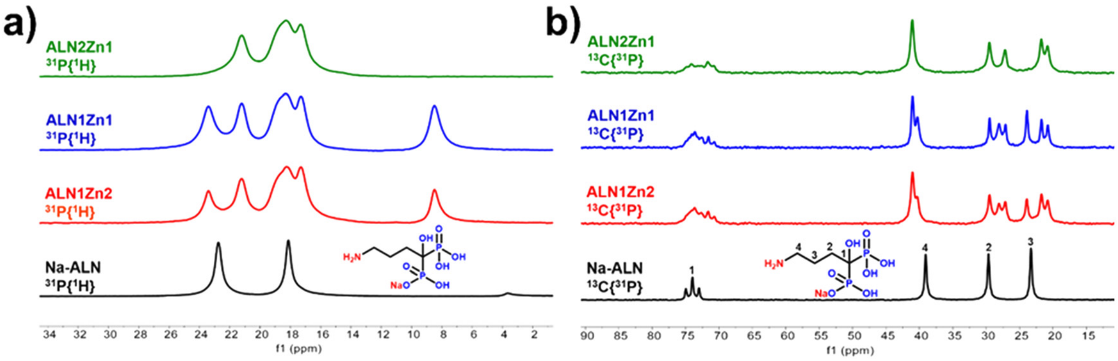

Fig. 4 CP-MAS NMR spectra of Na-ALN and ossified zinc alendronate catalysts, (a) ^{31}P, (b) ^{13}C.

(using a CO_2 surrogate). The catalytic activities of zinc nitrate and bare sodium alendronate were also investigated under the same reaction conditions to compare the advancement gained using the ossified zinc alendronate. The desired product, 4-(hydroxymethyl)-1,3-dioxolan-2-one (glycerol carbonate, denoted as $GlyCO_3$), generated *via* glycerol valorization using urea as a CO_2 surrogate, was generated *via* the initially formed 2,3-dihydroxypropyl carbamate (glycerol carbamate) intermediate (IM)^{26,79} (Scheme 2). Typically, (2-oxo-1,3-dioxolan-4-yl)methyl carbamate (A), 1-((2-oxo-1,3-dioxolan-4-yl)methyl) urea (A′) and 4-((2,3-dihydroxypropoxy) methyl)-1,3-dioxolan-2-one (B) were detected as byproducts (Scheme 2). These compounds are believed to result from additional side reactions involving $GlyCO_3$ with residual urea and glycerol, respectively. Additionally, the dehydration and subsequent reaction of the available carbamate intermediate (IM) resulted in the formation of 4-(hydroxymethyl)oxazolidin-2-one (C) and oxybis(2-hydroxypropane-3,1-diyl)dicarbamate (D) as byproducts (Scheme 2) during the glycerolysis of urea, respectively. In addition to these, other byproducts analogous to those previously reported were detected. A thorough GC-MS/MS analysis of the reaction mixtures provided this information, and the MS spectra are provided in the SI.

The control reaction, without any added catalyst, resulted in 55.3% conversion of glycerol with 40.8% $GlyCO_3$ selectivity (Fig. 5a) and a 22.6% yield. The formation of side products was substantial (59.2%) at 140 °C after 7 h (Fig. 5a). When zinc nitrate was utilized as a catalyst, 88.9% glycerol conversion was achieved with an exceptional $GlyCO_3$ selectivity of 98.1%, and the selectivity of the side products was 1.9% at 140 °C for 7 h (Fig. 5a). Zinc nitrate was initially homogeneous in the reaction mixture at 140 °C. However, after 7 h of the reaction, it was transformed into a white powder. The white powder was analyzed using FT-IR and PXRD and was found to be zinc glycerolate (Fig. S11). Na-ALN facilitated a glycerol conversion of 66.3% and a $GlyCO_3$ selectivity of 92.3% with 7.7% byproduct selectivity (Fig. 5a) under the same reaction conditions and remained completely homogeneous in the reaction mixture. These findings suggest the potential applications of the ossification technique for the synthesis of reusable heterogeneous catalysts.

The catalytic performances of the ossified zinc alendronate catalysts with varying catalyst loadings of 5%, 10%, and 15% (w/w, relative to glycerol) at 140 °C for 7 h were examined, and the results are summarized in Fig. 5b and c. As shown in Fig. 5b and c, ALN1Zn2 achieved the highest conversion (77.9%) and excellent $GlyCO_3$ selectivity (95.1%) at a 10% catalyst loading, yielding 74.1% $GlyCO_3$. However, the catalyst performance declined by 24.4% and 23% in terms of conversion and 11.9% and 29.2% in terms of $GlyCO_3$ selectivity at 5% and 15% catalyst loadings, respectively. A catalyst loading of 10% showed the most balanced performance in terms of glycerol

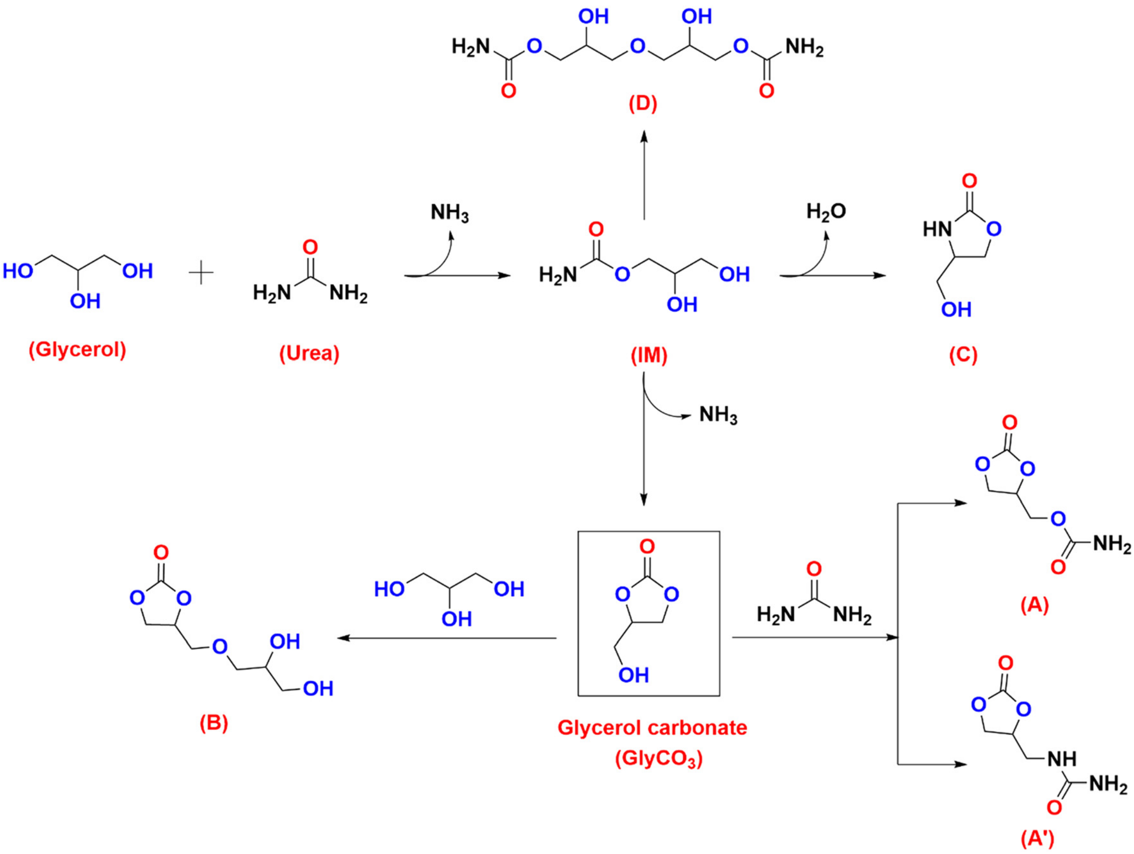

Scheme 2 Targeted product and byproducts from the glycerolysis of urea.

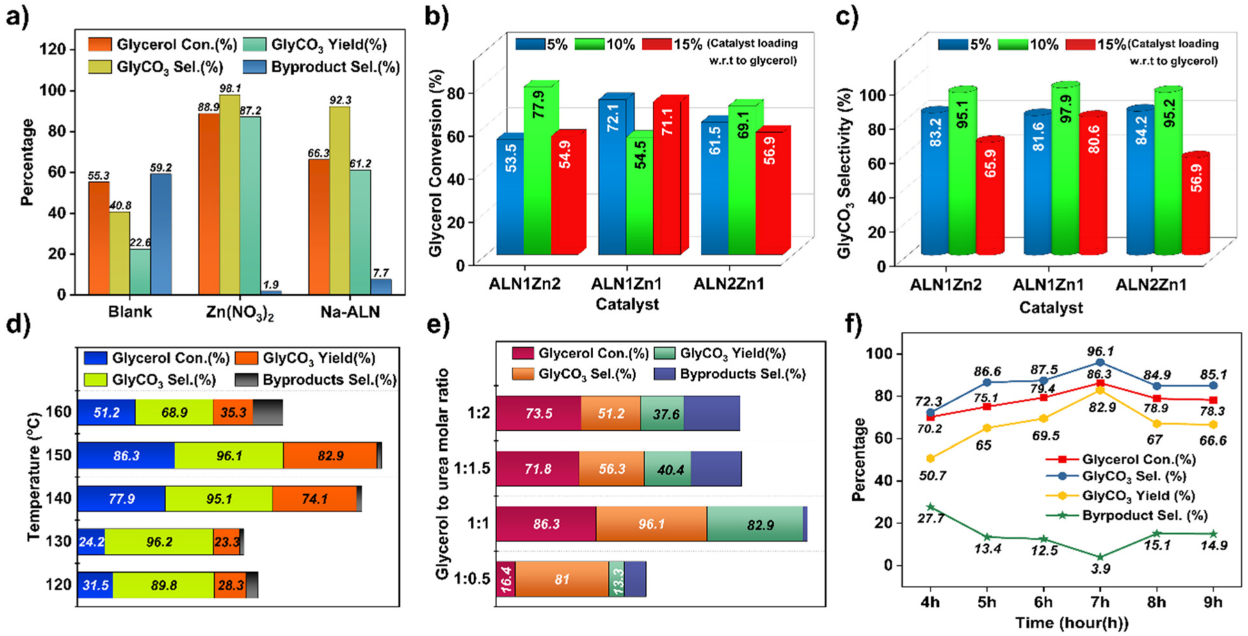

Fig. 5 a) Performance comparison of the blank (without catalyst), zinc nitrate and Na-ALN (140 °C for 7 h; catalyst loading = 10% (w.r.t. glycerol), G : U = 1 : 1). Effect of the ossified catalyst loading on the b) glycerol conversion and c) GlyCO$_3$ selectivity (140 °C, 7 h, G : U = 1 : 1). d) Temperature optimization using ALN1Zn2 (catalyst loading = 10%, 7 h, G : U = 1 : 1). e) Glycerol to urea ratio optimization using ALN1Zn2 (catalyst loading = 10%, 150 °C, 7 h; N$_2$ flow, 700 rpm). f) Reaction progress and evaluation of ALN1Zn2 with respect to time (150 °C, catalyst loading = 10%, G : U = 1 : 1, N$_2$ flow, 700 rpm).

conversion and GlyCO$_3$ selectivity for most formulations. Notably, this is likely due to the typical oversaturation of active sites at lower and higher catalyst loadings, respectively. The enhanced catalytic activity of ALN1Zn2 with a 10% loading can be ascribed to the increased surface density of the active zinc-phosphate species, as evidenced by the XPS surface concentration analysis. The highest activity demonstrated by ALN1Zn2 is attributed to the high comparative zinc availability in ALN1Zn2 and the consequent higher acidity. Therefore, ALN1Zn2 with a 10% loading was selected for subsequent studies.

The effect of the reaction temperature on the ALN1Zn2 (10% catalyst loading) performance after 7 h was evaluated by varying the temperature from 120 to 160 °C, and the data are presented in Fig. 5d. Increasing the reaction temperature from 120 °C to 150 °C increased glycerol conversion to 86.3% with a GlyCO$_3$ selectivity of 96.1% (82.9% GlyCO$_3$ yield). However, with a further increase in temperature to 160 °C, the catalytic performance decreased significantly (Fig. 5d). At 160 °C, the reaction mixture became highly viscous, sticky, and brown, indicating possible polymerization or thermal degradation of the reactants and products. Therefore, the optimal results were obtained at 150 °C in terms of conversion and selectivity (Fig. 5d).

Fig. 5e shows the influence of the glycerol-to-urea molar ratio on ALN1Zn2 (at 10% loading) at 150 °C after 7 h. The experimental results revealed that at an equimolar glycerol to urea ratio (G : U = 1 : 1), the conversion of glycerol reached 86.3%, with a GlyCO$_3$ selectivity of 96.1% and a yield of 82.9%. Deviations from this optimal ratio, whether increasing (1 : 1.5 and 1 : 2) or decreasing (1 : 0.5) the urea content, resulted in diminished glycerol conversion, GlyCO$_3$ selectivity, and consequently, overall yield. At higher urea concentrations (1 : 1.5 and 1 : 2), notable selectivity toward byproducts C and D was observed. Along with that, an extended polymeric product from excess urea was observed (MS data from GC-MS/MS analysis is given in the SI). In this case, the colour of the reaction mixture was brown, and the reaction mixture was sticky. Conversely, the equimolar ratio yielded minimal byproducts, indicating that ALN1Zn2 at 150 °C effectively activated the reactants, promoting the formation of the target product, GlyCO$_3$, *via* the IM. The presence of byproducts A and B in the 1 : 1 molar ratio scenario was attributed to GlyCO$_3$ reacting with residual urea and glycerol, respectively.

The overall progress of the reaction at 150 °C with a 1 : 1 glycerol to urea ratio was monitored over an extended reaction time, and the results are illustrated in Fig. 5f. GlyCO$_3$ selectivity demonstrated fluctuations over time. During the initial 7 h, glycerol conversion and GlyCO$_3$ selectivity increased and byproduct formation decreased as GlyCO$_3$ selectivity increased. However, after 7 h, a marked decline in the conversion and selectivity of GlyCO$_3$ was observed, coinciding with an increase in side product generation.

The recyclability of the catalyst was investigated under the optimized reaction conditions for a total of four consecutive cycles, including the initial use, as depicted in Fig. 6. Following each cycle, the spent catalyst was filtered and washed with methanol to remove any residual reactants/products from the catalyst surface, followed by drying in an oven prior to utilization in the subsequent cycle. From the initial reaction to consecutive recycles, a slight decrease in conversion and selectivity was observed, which can be

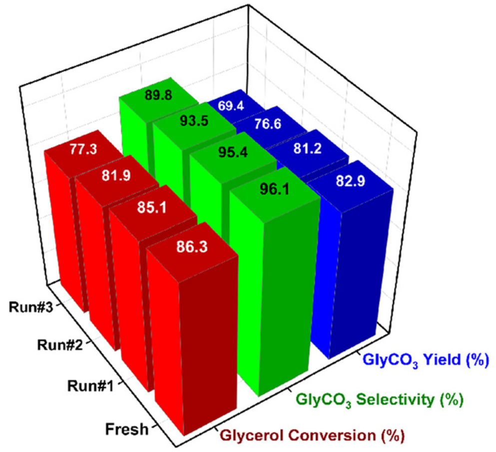

Fig. 6 Recycle run of ALN1Zn2 at 150 °C in 7 h, catalyst loading = 10 %, G : U = 1 : 1, N_2 flow, 700 rpm.

attributed to the loss of the catalyst while handling the catalyst between recycles. A marginal reduction in the catalyst activity might also be due to glycerol adsorption on the active sites of the catalyst and/or the formation of phosphate esters[9,94] with glycerol. Additionally, after each cycle, the stability of the spent catalyst was analyzed using FT-IR, PXRD, and XPS (Fig. S12–S15). All analyses yielded results similar to those of the fresh catalyst. The zinc content of the catalyst was also monitored by AAS (Table S3). The results indicated that the zinc content remained relatively consistent after the first recycling. This indicates that the handling losses may have contributed to the observed decrease in the glycerol conversion. These findings indicate that the ALN1Zn2 catalyst is stable and reusable for the alcoholysis of urea with glycerol.

ALN1Zn2 is a well-rounded catalyst synthesized in a single step for the conversion of glycerol to $GlyCO_3$ owing to its excellent performance, simple synthesis procedure, and sustainable characteristics. ALN1Zn2 distinguishes itself from the other catalysts, as shown in Table 5, through its use of economical and ecofriendly starting materials, even though some catalysts achieve higher turnover numbers (TONs) and turnover frequencies (TOFs). The catalyst 2.5 wt% Au/MgO achieves a remarkable TOF of 946 h^{-1} but requires costly noble metals, whereas ALN1Zn2 presents itself as a more affordable solution (Table 5). ALN1Zn2 presents practical advantages for large-scale applications owing to its simple preparation process, in contrast to Zn/MCM-41 (im), which requires complex procedures to achieve a high TON of 1275 (Table 5). ALN1Zn2 was extensively characterized to provide a deep mechanistic understanding of its catalytic properties, despite its moderate TON and TOF values, which are essential for future catalyst development. ALN1Zn2 combines multiple strengths, establishing it as a viable and user-friendly catalyst for sustainable glycerol carbonate production.

The progress of $GlyCO_3$ formation during glycerol valorization with urea was investigated using FT-IR spectroscopy to monitor the temporal changes in the functional groups. The FT-IR spectra of the reaction mixture at specific time intervals using ossified ALN1Zn2 are illustrated in Fig. 7 and S16. Fig. 7a explains the functional group assignments in the reaction pathway. A marked decrease in the characteristic peaks associated with C═O stretching and N–H bending of urea[26] (1611 and 1657 cm^{-1}, Fig. 7a) was observed as urea decomposed

Table 5 Competitive study of the glycerolysis of urea

Catalyst	Temp. (°C)	Rxn time (h)	Gly. con. (%)	$GlyCO_3$ sel. (%)	$GlyCO_3$ yield (%)	Cat. loading (wt%)	TON	TOF (h^{-1})	Cat. syn. steps	Total usage cycle
ALN1Zn2	150	7	86.3	96.1	82.9	10	53	7.6	1	4
Fe–ZnO QDs[80]	150	4	90.7	100	90.6	5	1.4	0.4	1	4
Gyp800 (ref. 79)	150	4	92.8	90.1	83.6	1.81	—	—	1	4
RG150 (ref. 81)	150	4	94.1	92.4	86.9	1.81	—	—	1	3
Co_3O_4/ZnO (ref. 82)	145	4	69	97	66.9	6	—	—	1	4
MoO_3/SnO_2 (ref. 19)	150	4	69	97	66.9	10	42.4	10.6	2	5
$Sn(OH)_2/(4.9\ Sn^{2+})$[83]	140	4	87	85	73.9	4.9 mol%	17.8	10.6	—	Reusable
Cu–Mn[84]	140	6	90.8	99	89.9	3	1961	326.8	2	5
15%WO_3/TiO_2 (ref. 85)	140	4	100	73	73	10	170	42.5	2	3
2.5 wt% Au/MgO (ref. 86)	150	4	80	70	56	1.8	3783	945.8	2	10
TaPC[10]	140	4	88	98	86.2	10	—	—	2	5
M1P3 (ref. 9)	140	4	95	99	94.1	5	—	—	2	5
SW21 (ref. 87)	140	4	52.1	95.3	49.7	10	—	—	2	4
Zn_1/NC[26]	120	6	94.8	95	89.7	5	225	37.5	3	5
Zn/MCM-41 (im)[88]	145	5	75	98	73.5	0.05	1275	255	3	4
Zn1TPA[14]	140	4	69.2	99.4	68.7	10	221	55.3	3	4
50%-$Zn_7Al_3O_x$/ARM[27]	140	5	69	90	62.1	5	—	—	3	—
In0.66TPA[89]	140	4	69.4	98.8	68.5	10	365	91.3	3	4
Ta0.4TPA[90]	140	4	71	100	71	10	—	—	3	4
Sm0.66TPA[91]	140	4	49.5	85.4	42.3	10	—	—	3	4
BNP@C-800 (ref. 92)	140	4	93.6	93.7	87.7	5	—	—	4	5
CS-550-P[93]	150	5	82	98	80.4	10	—	—	5	5

Temp: temperature, Rxn: reaction, Gly: glycerol, Con.: conversion, Sel.: selectivity, Cat.: catalyst, Syn.: synthesis.

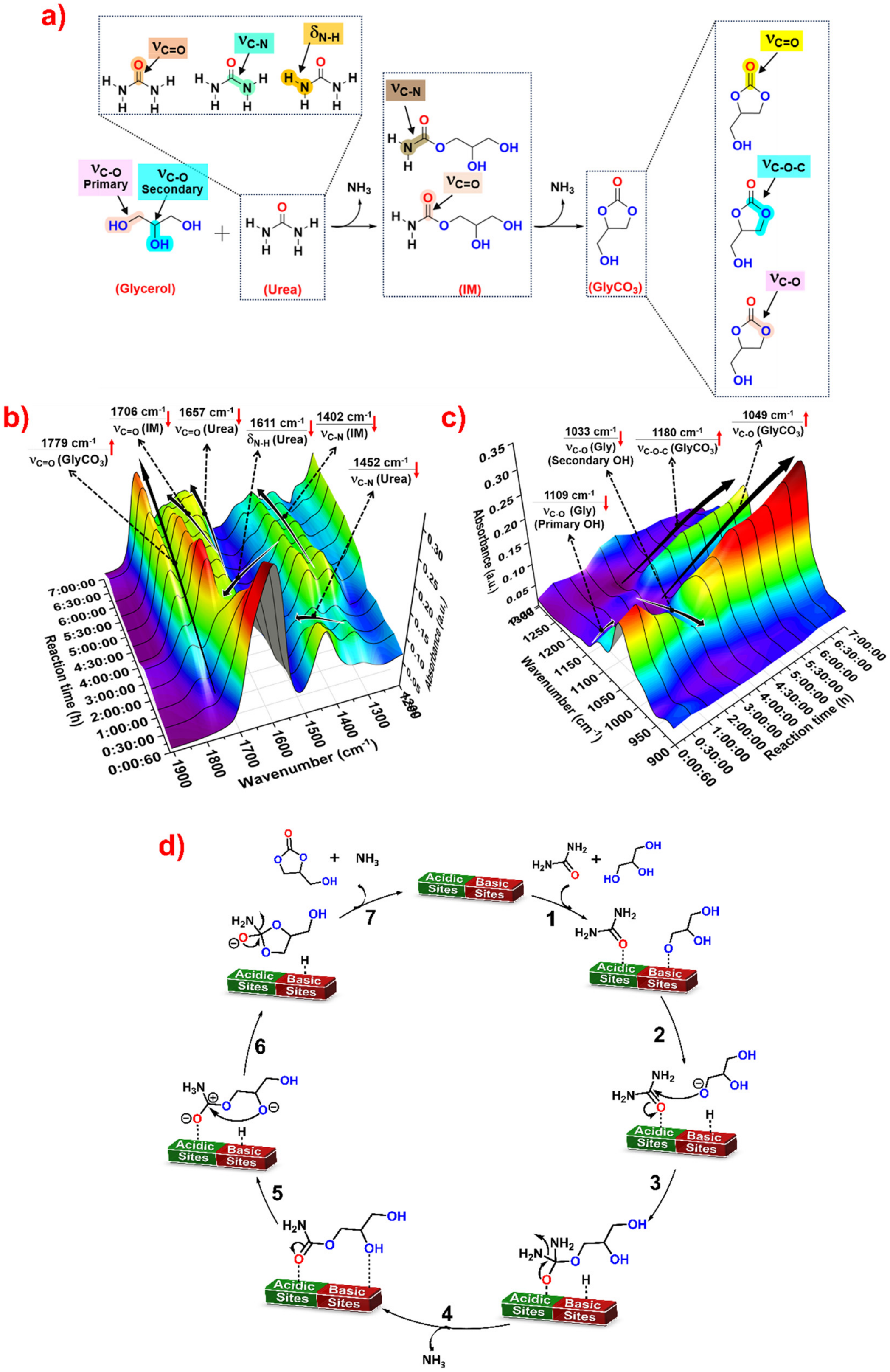

Fig. 7 a) Reaction pathway and functional group assignment in the synthesis of GlyCO$_3$. b) and c) 3-Dimensional spectra of the glycerolysis of urea monitored over ALN1Zn2 (catalyst loading = 10%, 150 °C, 7 h, G : U = 1 : 1, N$_2$ flow, 700 rpm). d) Plausible mechanism of GlyCO$_3$ synthesis from urea and glycerol on the ALN1Zn2 catalyst surface.

into isocyanic acid (HNCO) and ammonia (NH_3). As the reaction proceeded, the intensity of the O–H stretching vibrations of glycerol (3300–3500 cm^{-1}) diminished, indicating hydroxyl group participation in the reaction and its consumption (Fig. S17). The emergence of C═O stretching from amide (1706 cm^{-1})[26] and C–N stretching vibrations (1402 cm^{-1})[26] signified the formation of the carbamate intermediate (IM) through the nucleophilic attack of the hydroxyl group of glycerol (Fig. 7b). Subsequently, the intramolecular cyclization of the carbamate IM was evidenced by the appearance of strong carbonyl absorbance (1779 cm^{-1},[26,92] Fig. 7b), symmetric and asymmetric carbonate ring stretching (1180 cm^{-1}), and the C–O stretching vibration (1049 cm^{-1}) of $GlyCO_3$, accompanied by a further reduction in the C–O stretching frequency (1033 cm^{-1}) of the secondary OH of glycerol (Fig. 7c). Notably, the carbamate intermediate (IM) concentration in the ALN1Zn2-catalyzed reaction mixture (Fig. 7b) initially increased and subsequently decreased over time, suggesting that the active acidic sites on the catalyst surface efficiently activated urea to rapidly form $GlyCO_3$ *via* the carbamate intermediate. Furthermore, unreacted urea and glycerol interacted with $GlyCO_3$ to produce byproducts A, A′, and B, respectively. The three-dimensional FT-IR spectra of glycerol valorization with urea, presented in Fig. 7b and c, offer more compelling evidence when examined alongside their corresponding two-dimensional spectra (Fig. S16 and S17).

To elucidate the role of active zinc in the catalyst skeleton, glycerol valorization was conducted utilizing bare Na-ALN as a catalyst with urea at 140 °C and a 1 : 1 glycerol-to-urea molar ratio. The observed glycerol conversion and $GlyCO_3$ selectivity were 66.3% and 92.4%, respectively. Furthermore, these materials (precursors to the ossified Zn-alendronate catalyst material) remained homogeneous during and after the reaction. These results indicate that the ossification of zinc with Na-ALN renders the catalyst heterogeneous, and the presence of active zinc on the catalyst surface plays a significant role in activating the reactants to form $GlyCO_3$, thus serving the two purposes of easy catalyst-product separation and enhanced activity, selectivity, and catalyst stability. The absence of the 2250 cm^{-1} N═C═O stretching band in the FT-IR spectra indicated that isocyanic acid was not the primary product of this reaction. The observations by Aresta *et al.* regarding phosphated zirconia catalysts exhibit a similar behaviour to these findings.[95] Their catalysts facilitate a reaction pathway involving the carbamate intermediate (IM) rather than proceeding through isocyanic acid, as observed in $ZnSO_4$-based systems. The significance of this distinction is that the formation of isocyanic acid and its oligomers reflects the nonselective use of urea.[86] Based on the FT-IR results of the reaction progress, the initial step of the reaction proceeded *via* carbamate formation with no evidence of competition with the formation of the isocyanate complex pathway. Careful observation of the preliminary experiments conducted in this study suggests that the role of the catalyst is linked to the slower second step of the reaction, specifically the intramolecular reaction forming the carbonate. Secondly, it is a well-established hypothesis that bifunctional catalysts with balanced acidic and basic sites perform the selective synthesis of $GlyCO_3$, which allows the coadsorption of urea and glycerol.[9,10,84,93]

NH_3-TPD and CO_2-TPD analyses revealed that the ossified ALN1Zn2 possessed strong acidic and basic sites in the catalyst skeleton. Consequently, based on a previous literature survey[9,26] and TPD analyses, a catalytic mechanism for glycerol valorization with urea as a CO_2 surrogate is proposed in Fig. 7d. The total acidic and basic sites on the catalyst surface are the result of the synergistic effect of the presence of active zinc alendronate species and unperturbed Na-ALN sites within/on the catalyst. A plausible reaction mechanism can be proposed based on the characteristic features of the ossified ALN1Zn2 catalyst, as shown in Fig. 7d. A urea molecule is preferentially adsorbed and activated at the acidic site, and glycerol is activated by the basic sites by proton abstraction (step 1). The basic sites initiate the deprotonation of the ortho hydroxyl group of glycerol to produce an RO^- nucleophile (step 2). The nucleophile targets the carbonyl group of the urea (step 2). The proton released from glycerol binds to the amino groups of urea (step 3) and releases an NH_3 molecule (step 4). The initial esterification process depends on NH_3 gas release, which forms a carbamate intermediate (IM) (step 4) while restoring the acid and base sites of the catalyst. The regenerated catalyst sites activate the C–O and –OH functional groups present in the intermediates (step 5), allowing intramolecular esterification to generate the final $GlyCO_3$ product with the elimination of another molecule of NH_3 (step 6). Finally, the $GlyCO_3$ molecule is desorbed from the surface of the catalyst, regenerating the catalyst for the next cycle (step 7).

Conclusion

The catalyst ALN1Zn2 was successfully synthesized using a single-step ossification technique and well characterized, using different techniques, for glycerol valorization with urea serving as a CO_2 substitute. Utilizing the ossification technique allowed the creation of heterogeneous catalysts that maintained stable, balanced acid-base properties. The catalyst ALN1Zn2 achieved the highest activity among the examined materials, with a glycerol conversion of 86.3% and a glycerol carbonate selectivity of 96.1% under the optimized testing conditions of 150 °C for 7 h using a 1 : 1 glycerol to urea ratio. ALN1Zn2 exhibited excellent performance consistency over multiple cycles while maintaining its catalytic activity with only slight degradation. The reaction mechanism involved a carbamate intermediate, according to mechanistic studies, while the catalyst promoted both urea activation and intramolecular cyclization. The straightforward preparation process, combined with cost-effective precursors and environmentally friendly features, positions these catalysts as viable options for extensive glycerol valorization operations.

Author contributions

Conceptualization: SBT, BRS; Methodology: SBT, BRS, Formal analysis: SBT, BRS; investigation: SBT, DB, DKR, data curation: SBT, DB, DKR, writing—original draft: SBT, writing—review and editing: DB, DKR, BRS, project administration: BRS.

Conflicts of interest

There are no conflicts to declare.

Data availability

All data supporting the findings of this study are provided within its supplementary information (SI). SI includes catalyst characterization, quantitative analysis of reaction products, identification of reaction products, DTA spectra, FESEM-EDS and HR-TEM images of catalysts, FT-EXAFS analysis table, XPS profile of catalysts, deconvoluted NH_3 and CO_2-TPD spectra, zinc glycerolate FT-IR and PXRD, spent catalyst study experiment and characterization of spent catalyst, experimental set up to study the reaction progress using FT-IR and its 2D spectra and available at DOI: [URL] (to be updated once accepted). Supplementary information is available. See DOI: https://doi.org/10.1039/d5cy01218j.

Acknowledgements

SBT acknowledges BITS Pilani for Research Fellowship, BRS acknowledges BITS Pilani, Pilani Campus for research infrastructure, Central Analytical Laboratory (CAL) and Sophisticated Instrumental Facility (SIF) BITS Pilani, Pilani Campus for materials characterization facilities and DST-FIST facility of the Department of Chemistry.

References

1 Y. Liu, B. Zhong and A. Lawal, Recovery and utilization of crude glycerol, a biodiesel byproduct, *RSC Adv.*, 2022, **12**(43), 27997–28008.
2 Biofuel production forecast by product type 2030, https://www.statista.com/statistics/1440696/biofuel-production-forecast-by-product-type/.
3 Glycerol Market Size, Global Trends 2025–2034, https://www.gminsights.com/industry-analysis/glycerol-market-size.
4 N. Yadav, G. Yadav and M. Ahmaruzzaman, Catalytic conversion and mechanism of glycerol into various value-added products: A critical review, *Ind. Crops Prod.*, 2024, **210**, 117999.
5 M. O. Sonnati, S. Amigoni, E. P. Taffin De Givenchy, T. Darmanin, O. Choulet and F. Guittard, Glycerol carbonate as a versatile building block for tomorrow: synthesis, reactivity, properties and applications, *Green Chem.*, 2013, **15**(2), 283–306.
6 Glycerol Carbonate Market 2024 - Global Insights, Growth, Trends & Forecast, https://www.reportsanddata.com/report-detail/glycerol-carbonate-market.
7 P. Koranian, Q. Huang, A. K. Dalai and R. Sammynaiken, Chemicals Production from Glycerol through Heterogeneous Catalysis: A Review, *Catalysts*, 2022, **12**, 897.
8 Y. Li, H. Liu, Z. Zheng, Z. Fu, D. He and Q. Zhang, Synthesis of Glycerol Carbonate via Alcoholysis of Urea with Glycerol: Current Status and Future Prospects, *Ind. Eng. Chem. Res.*, 2022, **61**(17), 5698–5711.
9 K. Bhaduri, A. Auroux, A. Bhaumik and B. Chowdhury, Bifunctional molybdenum phosphate catalyst with tunable acidity–basicity for the sustainable synthesis of glycerol carbonate via solvent-free carbonylation of glycerol with urea, *Appl. Organomet. Chem.*, 2022, **36**(12), e6904.
10 K. Bhaduri, A. Ghosh, A. Auroux, S. Chatterjee, A. Bhaumik and B. Chowdhury, Soft-templating routes for the synthesis of mesoporous tantalum phosphates and their catalytic activity in glycerol dehydration and carbonylation reactions, *Mol. Catal.*, 2022, **518**, 112074.
11 P. Zhang, L. Liu, M. Fan, Y. Dong and P. Jiang, The value-added utilization of glycerol for the synthesis of glycerol carbonate catalyzed with a novel porous ZnO catalyst, *RSC Adv.*, 2016, **6**(80), 76223–76230.
12 H. Nguyen-Phu, L. T. Do and E. W. Shin, Investigation of glycerolysis of urea over various ZnMeO (Me = Co, Cr, and Fe) mixed oxide catalysts, *Catal. Today*, 2020, **352**, 80–87.
13 S. E. Kondawar, R. B. Mane, A. Vasishta, S. B. More, S. D. Dhengale and C. V. Rode, Carbonylation of glycerol with urea to glycerol carbonate over supported Zn catalysts, *Appl. Petrochem. Res.*, 2017, **7**(1), 41–53.
14 K. Jagadeeswaraiah, C. R. Kumar, P. S. S. Prasad and N. Lingaiah, Incorporation of Zn2+ ions into the secondary structure of heteropoly tungstate: catalytic efficiency for synthesis of glycerol carbonate from glycerol and urea, *Catal. Sci. Technol.*, 2014, **4**(9), 2969–2977.
15 J. H. Park, J. S. Choi, S. K. Woo, S. D. Lee, M. Cheong, H. S. Kim and H. Lee, Isolation and characterization of intermediate catalytic species in the Zn-catalyzed glycerolysis of urea, *Appl. Catal., A*, 2012, **433–434**, 35–40.
16 L. Wang, Y. Ma, Y. Wang, S. Liu and Y. Deng, Efficient synthesis of glycerol carbonate from glycerol and urea with lanthanum oxide as a solid base catalyst, *Catal. Commun.*, 2011, **12**(15), 1458–1462.
17 D. Wang, X. Zhang, C. Liu and T. Cheng, Synthesis of glycerol carbonate from glycerol and urea over lanthanum compounds, *React. Kinet., Mech. Catal.*, 2015, **115**(2), 597–609.
18 J. Zhang and D. He, Lanthanum-based mixed oxides for the synthesis of glycerol carbonate from glycerol and urea, *React. Kinet., Mech. Catal.*, 2014, **113**(2), 375–392.
19 B. Mallesham, A. Rangaswamy, B. G. Rao, T. V. Rao and B. M. Reddy, Solvent-Free Production of Glycerol Carbonate from Bioglycerol with Urea Over Nanostructured Promoted SnO_2 Catalysts, *Catal. Lett.*, 2020, **150**(12), 3626–3641.

20 A. Srikanth, B. Viswanadham, V. P. Kumar, R. A. Nageswara and K. V. R. Chary, Synthesis and characterization of Cs-exchanged heteropolyacid catalysts functionalized with Sn for carbonolysis of glycerol to glycerol carbonate, *Appl. Petrochem. Res.*, 2016, **6**(2), 145–153.

21 J. Chen, C. Wang, B. Dong, W. Leng, J. Huang, R. Ge and Y. Gao, Ionic liquids as eco-friendly catalysts for converting glycerol and urea into high value-added glycerol carbonate, *Chin. J. Catal.*, 2015, **36**(3), 336–343.

22 D. Wang, X. Zhang, X. Cong, S. Liu and D. Zhou, Influence of Zr on the performance of Mg-Al catalysts via hydrotalcite-like precursors for the synthesis of glycerol carbonate from urea and glycerol, *Appl. Catal., A*, 2018, **555**, 36–46.

23 V. P. Indran, A. S. H. Saud, G. P. Maniam, Y. H. Taufiq-Yap and M. H. Ab. Rahim, Viable Glycerol Carbonate Synthesis Through Direct Crude Glycerol Utilization from Biodiesel Industry, *Waste Biomass Valoriz.*, 2017, **8**(4), 1049–1059.

24 L. Zhang, Z. Zhang, C. Wu, Q. Qian, J. Ma, L. Jiang and B. Han, Microwave assisted synthesis of glycerol carbonate from glycerol and urea, *Pure Appl. Chem.*, 2017, **90**, 1–6.

25 S. I. Fujita, Y. Yamanishi and M. Arai, Synthesis of glycerol carbonate from glycerol and urea using zinc-containing solid catalysts: A homogeneous reaction, *J. Catal.*, 2013, **297**, 137–141.

26 J. Shi, Y. Cui, H. Sun, H. Wang, C. Liu and X. Xue, *et al.*, N-doped porous carbon-anchored zinc single-atom as an efficient and robust heterogeneous catalyst for glycerol carbonylation with urea, *Chem. Eng. J.*, 2023, **466**, 143317.

27 H. Nguyen-Phu, C.-yi Park and E. W. Shin, Activated red mud-supported Zn/Al oxide catalysts for catalytic conversion of glycerol to glycerol carbonate: FTIR analysis, *Catal. Commun.*, 2016, **85**, 52–56.

28 H. Nguyen-Phu, C.-yi Park and E. W. Shin, Dual catalysis over ZnAl mixed oxides in the glycerolysis of urea: Homogeneous and heterogeneous reaction routes, *Appl. Catal., A*, 2018, **552**, 1–10.

29 T. W. Turney, A. Patti, W. Gates, U. Shaheen and S. Kulasegaram, Formation of glycerol carbonate from glycerol and urea catalysed by metal monoglycerolates, *Green Chem.*, 2013, **15**(7), 1925–1931.

30 Y. P. Zhu, T. Y. Ma, Y. L. Liu, T. Z. Ren and Z. Y. Yuan, Metal phosphonate hybrid materials: from densely layered to hierarchically nanoporous structures, *Inorg. Chem. Front.*, 2014, **1**(5), 360–383.

31 A. Dutta, M. Pramanik, A. K. Patra, M. Nandi, H. Uyama and A. Bhaumik, Hybrid porous tin(iv) phosphonate : an efficient catalyst for adipic acid synthesis and a very good adsorbent for CO_2 uptake, *Chem. Commun.*, 2012, **48**(53), 6738–6740.

32 T. Kimura, A New Family of Nonsiliceous Porous Hybrids from Bisphosphonates, *J. Nanosci. Nanotechnol.*, 2013, **13**(4), 2461–2470.

33 T. Y. Ma and S. Z. Qiao, Acid-base bifunctional periodic mesoporous metal phosphonates for synergistically and heterogeneously catalyzing CO_2 conversion, *ACS Catal.*, 2014, **4**(11), 3847–3855.

34 X. W. Lv, C. C. Weng, Y. P. Zhu and Z. Y. Yuan, Nanoporous Metal Phosphonate Hybrid Materials as a Novel Platform for Emerging Applications: A Critical Review, *Small*, 2021, **17**(22), 2005304.

35 T. Y. Ma and Z. Y. Yuan, Metal Phosphonate Hybrid Mesostructures: Environmentally Friendly Multifunctional Materials for Clean Energy and Other Applications, *ChemSusChem*, 2011, **4**(10), 1407–1419.

36 T. Y. Ma, L. Liu, Q. F. Deng, X. Z. Lin and Z. Y. Yuan, Increasing the H + exchange capacity of porous titanium phosphonate materials by protecting defective P–OH groups, *Chem. Commun.*, 2011, **47**(21), 6015–6017.

37 B. R. Sarkar and R. V. Chaudhari, Ossification: A new approach to immobilize metal complex catalysts-applications to carbonylation and Suzuki coupling reactions, *J. Catal.*, 2006, **242**(1), 231–238.

38 X. Mo, J. Qian, Y. Chen, W. Zhang, P. Xian and S. Tang, *et al.*, Corrosion and degradation decelerating alendronate embedded zinc phosphate hybrid coating on biodegradable Zn biomaterials, *Corros. Sci.*, 2021, **184**, 109398.

39 N. Finkelstein, R. Lidor-Hadas and J. Aronhime, Hydrate forms of alendronate sodium, processes for manufacture thereof, and pharmaceutical compositions thereof, *US Pat.*, 6281381 B1, Teva Pharmaceutical Industries Ltd., 2001.

40 B. Sienkiewicz, P. Kowalski, K. Ossowska, J. Potok, B. Cetina-Cizmek, M. Horvat, P. Tudja and A. Danilovski, Solid-state form of alendronate sodium and preparation thereof, *US Pat.*, 20050113343 A1, Pliva – Research and Development, Ltd., 2005.

41 S. Hachani and L. Guerbous, Synthesis, Luminescence, and Energy Transfer Properties of YPO_4:Gd^{3+}, Eu^{3+} and YP_3O_9: Sm^{3+}, Eu^{3+} Phosphors, *J. Fluoresc.*, 2019, **29**, 665–672.

42 W. Maniukiewicz, J. Bojarska and L. Sieroń, Analysis of supramolecular interactions in alendroniate alkali metal salts: synthesis, structure, and properties of novel sodium alendronate polymorph, *Struct. Chem.*, 2018, **29**(5), 1525–1531.

43 L. Berzina-Cimdina and N. Borodajenko, Research of Calcium Phosphates Using Fourier Transform Infrared Spectroscopy, in *Infrared Spectroscopy - Materials Science, Engineering and Technology*, ed. T. Theophanides, InTech, 2012, ch. 6, pp. 123–148.

44 S. Chen, Z. Luo, L. Wu, C. Xie and X. Xiao, Amino-Modified Polylactic Acid Nanofibre Microspheres as Drug Sustained Release Carriers for Alendronate, *Polym.-Plast. Technol. Eng.*, 2018, **57**(18), 1873–1881.

45 M. Zvekic, L. C. Richards, C. C. Tong and E. T. Krogh, Characterizing photochemical ageing processes of microplastic materials using multivariate analysis of infrared spectra, *Environ. Sci.: Processes Impacts*, 2022, **24**(1), 52–61.

46 G. Ananchenko, J. Novakovic and A. Tikhomirova, Alendronate Sodium, in *Profiles of Drug Substances, Excipients and Related Methodology*, Academic Press Inc., 2013, ch. 1, vol. 38, pp. 1–33.

47 Y. S. Rammah, F. I. El-Agawany, K. A. Mahmoud, R. El-Mallawany, E. Ilik and G. Kilic, FTIR, UV–Vis–NIR spectroscopy, and gamma rays shielding competence of novel ZnO-doped vanadium borophosphate glasses, *J. Mater. Sci.: Mater. Electron.*, 2020, **31**(12), 9099–9113.

48 Y. Xing, B. Yan, Z. Yuan and K. Sun, Mesoporous tantalum phosphates: Preparation, acidity and catalytic performance for xylose dehydration to produce furfural, *RSC Adv.*, 2016, **6**(64), 59081–59090.

49 M. A. Marzouk, F. H. ElBatal and H. A. ElBatal, Investigation of ZnO-P_2O_5 Glasses Containing Variable Bi_2O_3 Contents Through Combined Optical, Structural, Crystallization Analysis and Interactions with Gamma Rays, *Silicon*, 2018, **10**(2), 615–625.

50 K. S. W. Sing, D. H. Everett, R. A. W. Haul, L. Moscou, R. A. Pierotti, J. Rouquerol and T. Siemieniewska, Reporting physisorption data for gas/solid systems with special reference to the determination of surface area and porosity, *Pure Appl. Chem.*, 1985, **57**, 603–619.

51 M. Thommes, K. Kaneko, A. V. Neimark, J. P. Olivier, F. Rodriguez-Reinoso and J. Rouquerol, *et al.*, Physisorption of gases, with special reference to the evaluation of surface area and pore size distribution (IUPAC Technical Report), *Pure Appl. Chem.*, 2015, **87**(9–10), 1051–1069.

52 V. G. Baldovino-Medrano, V. Niño-Celis and R. I. Giraldo, Systematic Analysis of the Nitrogen Adsorption-Desorption Isotherms Recorded for a Series of Materials Based on Microporous-Mesoporous Amorphous Aluminosilicates Using Classical Methods, *J. Chem. Eng. Data*, 2023, **68**(9), 2512–2528.

53 M. C. Biesinger, Accessing the robustness of adventitious carbon for charge referencing (correction) purposes in XPS analysis: Insights from a multi-user facility data review, *Appl. Surf. Sci.*, 2022, **597**, 153681.

54 J. G. Acheson, L. Robinson, S. Mckillop, S. Wilson, M. J. Mcivor and B. J. Meenan, *et al.*, TOFSIMS and XPS characterisation of strontium in amorphous calcium phosphate sputter deposited coatings, *Mater. Charact.*, 2021, **171**, 110739.

55 G. Lee, D. B. Go and C. P. O'Brien, Nonthermal Plasma-Stimulated C-N Coupling from CH_4 and N_2 Depends on the Presence of Surface CH_x and Plasma-Phase CN Species, *ACS Appl. Mater. Interfaces*, 2024, **16**(22), 28367–28378.

56 Q. Wang, L. Kong, J. Xu, B. Zhou, X. Liu and Z. Lin, *et al.*, Dual-Driven Interfaces of a CoP/CoO Cocatalyst on a Host Photocatalyst for Rapid Charge Transport in Solar-Driven H2 Evolution, *ACS Sustainable Chem. Eng.*, 2024, **12**(31), 11717–11727.

57 A. M. Puziy, O. I. Poddubnaya, R. P. Socha, J. Gurgul and M. Wisniewski, XPS and NMR studies of phosphoric acid activated carbons, *Carbon*, 2008, **46**, 2113–2123.

58 *NIST X-ray Photoelectron Spectroscopy Database*, 2024, https://srdata.nist.gov/xps/SpectraIdentifier.

59 M. R. Saeb, M. Ghaffari, H. Rastin, H. A. Khonakdar, F. Simon and F. Najafi, *et al.*, Biowaste chicken eggshell powder as a potential cure modifier for epoxy/anhydride systems: competitiveness with terpolymer-modified calcium carbonate at low loading levels, *RSC Adv.*, 2017, **7**(4), 2218–2230.

60 I. Gouzman, M. Dubey, M. D. Carolus, J. Schwartz and S. L. Bernasek, Monolayer vs. multilayer self-assembled alkylphosphonate films: X-ray photoelectron spectroscopy studies, *Surf. Sci.*, 2006, **600**(4), 773–781.

61 W. Chu, Y. Huang, C. Yang, Y. Liao, X. Zhang and M. Yan, *et al.*, Calcium phosphate nanoparticles functionalized with alendronate-conjugated polyethylene glycol (PEG) for the treatment of bone metastasis, *Int. J. Pharm.*, 2017, **516**(1–2), 352–363.

62 J. Ederer, P. Janoš, P. Ecorchard, J. Tolasz, V. Štengl and H. Beneš, *et al.*, Determination of amino groups on functionalized graphene oxide for polyurethane nanomaterials: XPS quantitation vs. functional speciation, *RSC Adv.*, 2017, **7**(21), 12464–12473.

63 Ž. Petrović, A. Šarić, I. Despotović, J. Katić, R. Peter and M. Petravić, *et al.*, Surface Functionalisation of Dental Implants with a Composite Coating of Alendronate and Hydrolysed Collagen: DFT and EIS Studies, *Materials*, 2022, **15**(15), 5127.

64 C. V. Waiman, J. M. Arroyave, H. Chen, W. Tan, M. J. Avena and G. P. Zanini, The simultaneous presence of glyphosate and phosphate at the goethite surface as seen by XPS, ATR-FTIR and competitive adsorption isotherms, *Colloids Surf., A*, 2016, **498**, 121–127.

65 K. S. Siow, L. Britcher, S. Kumar and H. J. Griesser, *et al.*, XPS Study of Sulfur and Phosphorus Compounds with Different Oxidation States, *Sains Malays.*, 2018, **47**(8), 1913–1922.

66 D. A. Torres-Ceron, S. Amaya-Roncancio, J. S. Riva, A. Vargas-Eudor, D. Escobar-Rincon and E. Restrepo-Parra, Incorporation of P^{5+} and P^{3-} from phosphate precursor in TiO_2:P coatings produced by PEO: XPS and DFT study, *Surf. Coat. Technol.*, 2021, **421**, 127437.

67 R. Shen, J. Xie, X. Lu, X. Chen and X. Li, Bifunctional Cu_3P Decorated g-C_3N_4 Nanosheets as a Highly Active and Robust Visible-Light Photocatalyst for H_2 Production, *ACS Sustainable Chem. Eng.*, 2018, **6**(3), 4026–4036.

68 G. Ge, S. Yuan, Q. Liu, D. Yang, J. Shi and X. Lan, *et al.* Insight into the function of noble-metal free Cu_3P decorated $Zn_{0.5}Cd_{0.5}S$ for enhanced photocatalytic hydrogen evolution under visible light irradiation–mechanism for continuous increasing activity, *Appl. Surf. Sci.*, 2022, **597**, 153660.

69 M. C. Biesinger, L. W. M. Lau, A. R. Gerson and R. S. C. Smart, Resolving surface chemical states in XPS analysis of first row transition metals, oxides and hydroxides: Sc, Ti, V, Cu and Zn, *Appl. Surf. Sci.*, 2010, **257**(3), 887–898.

70 S. Bera, A. A. M. Prince, S. Velmurugan, P. S. Raghavan, R. Gopalan and G. Panneerselvam, *et al.*, Formation of zinc ferrite by solid-state reaction and its characterization by XRD and XPS, *J. Mater. Sci.*, 2001, **36**(22), 5379–5384.

71 B. R. Strohmeier, Zinc Aluminate (ZnAl2O4) by XPS, *Surf. Sci. Spectra*, 1994, **3**(2), 128–134.

72 P. Druska, U. Steinike and V. Šepelák, Surface Structure of Mechanically Activated and of Mechanosynthesized Zinc Ferrite, *J. Solid State Chem.*, 1999, **146**(1), 13–21.

73 B. Chakraborty, A. Indra, P. V. Menezes, M. Driess and P. W. Menezes, Improved chemical water oxidation with Zn in the tetrahedral site of spinel-type $ZnCo_2O_4$ nanostructure, *Mater. Today Chem.*, 2020, **15**, 100226.

74 T. Yan, W. Bing, M. Xu, Y. Li, Y. Yang and G. Cui, Acid-base sites synergistic catalysis over Mg-Zr-Al mixed metal oxide toward synthesis of diethyl carbonate, *RSC Adv.*, 2018, **8**, 4695–4702.

75 F. Arena, R. Dario and A. Parmaliana, A characterization study of the surface acidity of solid catalysts by temperature programmed methods, *Appl. Catal., A*, 1998, **170**(1), 127–137.

76 L. Xu, D. He, L. Liu, T. Pei and J. Ren, Effect of precursor on the performance of phosphate-modified g-Al_2O_3 catalysts for the dehydration of methanol, *RSC Adv.*, 2015, **5**, 92628–92633.

77 F. C. Jentoft, Solid Acids and Bases, in *Comprehensive Inorganic Chemistry II (Second Edition): From Elements to Applications*, Elsevier Ltd, 2013, pp. 205–230.

78 T. Ishii and T. Kyotani, Temperature Programmed Desorption, in *Materials Science and Engineering of Carbon: Characterization*, Elsevier, 2016 ch. 14, pp. 287–305.

79 M. H. Mohd, N. A. S. Zuhaimi, A. S. Saud, V. R. Madduluri, H. Alshammari and G. P. Maniam, Synthesis of glycerol carbonate from industrial by-products by alcoholysis of urea: Crude glycerol and red gypsum, *Fuel*, 2024, **357**, 129774.

80 T. Butburee, A. Prasert, B. Rungtaweevoranit, P. Khemthong, P. Mano and S. Youngjan, *et al.*, Engineering Lewis-Acid Defects on ZnO Quantum Dots by Trace Transition-Metal Single Atoms for High Glycerol-to-Glycerol Carbonate Conversion, *Small*, 2024, **20**, 2403661.

81 N. A. S. Zuhaimi, V. P. Indran, M. A. Deraman, N. F. Mudrikah, G. P. Maniam and Y. H. Taufiq-Yap, *et al.*, Reusable gypsum based catalyst for synthesis of glycerol carbonate from glycerol and urea, *Appl. Catal., A*, 2015, **502**, 312–319.

82 F. Rubio-Marcos, V. Calvino-Casilda, M. A. Bañares and J. F. Fernandez, Novel hierarchical Co_3O_4/ZnO mixtures by dry nanodispersion and their catalytic application in the carbonylation of glycerol, *J. Catal.*, 2010, **275**(2), 288–293.

83 D. M. Chaves and M. J. Da Silva, A selective synthesis of glycerol carbonate from glycerol and urea over $Sn(OH)_2$: A solid and recyclable: In situ generated catalyst, *New J. Chem.*, 2019, **43**(9), 3698–3706.

84 W. Luo, L. Sun, Y. Yang, Y. Chen, Z. Zhou and J. Liu, *et al.*, Cu-Mn composite oxides: Highly efficient and reusable acid-base catalysts for the carbonylation reaction of glycerol with urea, *Catal. Sci. Technol.*, 2018, **8**(24), 6468–6477.

85 K. Jagadeeswaraiah, C. Ramesh Kumar, A. Rajashekar, A. Srivani and N. Lingaiah, The Role of Tungsten Oxide Species Supported on Titania Catalysts for the Synthesis of Glycerol Carbonate from Glycerol and Urea, *Catal. Lett.*, 2016, **146**(3), 692–700.

86 C. Hammond, J. A. Lopez-Sanchez, M. Hasbi Ab Rahim, N. Dimitratos, R. L. Jenkins and A. F. Carley, *et al.*, Synthesis of glycerol carbonate from glycerol and urea with gold-based catalysts, *Dalton Trans.*, 2011, **40**(15), 3927–3937.

87 K. Jagadeeswaraiah, C. R. Kumar, P. S. S. Prasad, S. Loridant and N. Lingaiah, Synthesis of glycerol carbonate from glycerol and urea over tin-tungsten mixed oxide catalysts, *Appl. Catal., A*, 2014, **469**, 165–172.

88 S. E. Kondawar, A. S. Potdar and C. V. Rode, Solvent-free carbonylation of glycerol with urea using metal loaded MCM-41 catalysts, *RSC Adv.*, 2015, **5**(21), 16452–16460.

89 M. S. Babu, A. Srivani, B. S. Rao and D. Ayodhya, Indium exchanged heteropoly tungstates: Efficient catalysts for the synthesis of glycerol carbonate from glycerol and urea, *Inorg. Chim. Acta*, 2023, **556**, 121655.

90 M. S. Babu, A. Srivani, G. Parameswaram, G. Veerabhadram and N. Lingaiah, Understanding the Role of Tantalum in Heteropoly Tungstate Catalysts for the Synthesis of Glycerol Carbonate from Glycerol and Urea, *Catal. Lett.*, 2015, **145**(9), 1784–1791.

91 C. R. Kumar, K. Jagadeeswaraiah, P. S. S. Prasad and N. Lingaiah, Samarium-exchanged heteropoly tungstate: An efficient solid acid catalyst for the synthesis of glycerol carbonate from glycerol and benzylation of anisole, *ChemCatChem*, 2012, **4**(9), 1360–1367.

92 H. Wang, Y. Cui, J. Shi, X. Tao and G. Zhu, Porous carbon supported Lewis acid-base sites as metal-free catalysts for the carbonylation of glycerol with urea, *Appl. Catal., B*, 2023, **330**, 122457.

93 K. Bhaduri, R. Chatterjee, A. Bhaumik and B. Chowdhury, Metal-Free Phosphate Modified Hierarchically Porous Carbon-Silica Nanocomposites for Solvent-Free Glycerol Carbonylation and Esterification Reactions, *ACS Sustainable Chem. Eng.*, 2022, **10**(34), 11242–11256.

94 R. Rodrigues, M. Gonçalves, D. Mandelli, P. P. Pescarmona and W. A. Carvalho, Solvent-free conversion of glycerol to solketal catalysed by activated carbons functionalised with acid groups, *Catal. Sci. Technol.*, 2014, **4**(8), 2293–2301.

95 M. Aresta, A. Dibenedetto, F. Nocito and C. Ferragina, Valorization of bio-glycerol: New catalytic materials for the synthesis of glycerol carbonate via glycerolysis of urea, *J. Catal.*, 2009, **268**(1), 106–114.